Numerical Study of Multiphase Flows with Temperature Effects

Zekang Cheng

Department of Engineering

University of Cambridge

First year report in
Division A

Supervised by

Dr. Jie Li

August, 2015

To people I love

Abstract

This report documents the development that has been made on the existing finite element method, including developing the isoparametric finite element method and solving the coupling of heat transfer and fluid motion. The effort is motivated by our specific research interest in non-isothermal multiphase flows. Heat transfer and temperature dependence of fluid properties have to be considered and direct numerical simulation of these flows requires a highly accurate interface representation.

The isoparametric method and the convection solver have been developed on a fixed mesh. Quantitative agreement with corresponding benchmark solution has been obtained and the method is validated. Better performance has been observed for isoparametric finite method compared with previous method with straight triangle edge. The improvement is attributed to the better representation of the curved boundaries: fitting the boundary with second-order curved segments rather than linear segments.

In addition, the proof is provided that there exists a static solution of a circular bubble in our numerical method. This will contribute to the suppression of spurious currents, which can lead to disastrous results in the simulation of multiphase flows.

Acknowledgements

Contents

Chapter 1

Introduction

1.1 Motivation

The term "multiphase flow" is used to refer to any fluid flow which consists of more than one phase or component (Brennen, 2005). The presence of the interface is the key character of multiphase flows. An interface is the boundary which distinguishes different phases. Many chemical and physical properties, including density and viscosity, undergo a value jump on the interface. The interface also possesses localised properties, the most prominent of which is the surface tension. The surface tension represents the magnitude of the force per unit length normal to a cut in the interface (Levich and Krylov, 1969) and it leads to the discontinuity of the stress tensor on the interface. In addition to all the discontinuities on the interface boundaries, the interface is not fixed in most multiphase flow problems. Hence, the shapes, locations and the evolution of the interfaces have to be coupled with the velocity fields and pressure, and all of these must be determined simultaneously (Davis, 2002).

When temperature is not a constant, the problem become more complicated. Not only heat transfer has to be considered, but also important fluid properties, density, viscosity and surface tension, are temperature dependent and therefore are variable spatially and temporally. Density variation leads to buoyancy force if gravity is taken into consideration. Shear stresses at the interface arise to balance

the surface tension gradients induced by the temperature field, resulting in fluid motion, and this is known as Marangoni effect (Scriven and Sternling, 1960). The effects of variable viscosity have not been studied much and therefore are still not clear.

(a) Basaran et al. (2013) (b) photo from Gatech Spray Lab
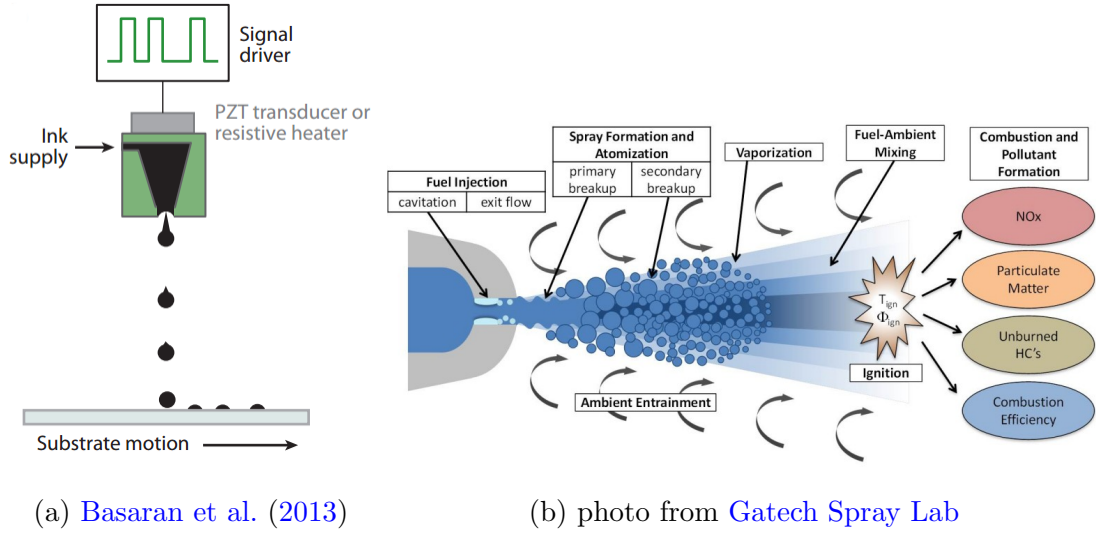
Figure 1.1: Schematic of (a) droplet-on-demand inkjet printing with piezo-electrically actuated or thermal inkjet methods and (b) diesel spray physical processes leading to ignition under high-temperature and pressure conditions.

Temperature effects indeed cause more technical difficulties, however, non-isothermal multiphase flows are more common in the real world compared with isothermal multiphase flows. They also play important roles in a wide range of industrial applications, examples including inkjet printing, atomisation in combustors and microfluidic actuation.

An inkjet printer is a device which ejects uniform droplets from microscopic nozzles and deposit them on the substrate (Basaran et al., 2013). Micro-droplets come from the breakup of a continuous ink jet. In the thermal inkjet printing method, the temperature differences between the nozzle and the substrate are relatively high. Jet breakup and droplet impact take place under non-isothermal circumstance. Hence, temperature effects are important in deciding the size and uniformity of droplet and whether ink-droplet impacts produce a splash.

In an automobile, fuel is firstly atomised and then injected into the combustion chamber (Zhao et al., 1999). Droplet collision and impact occur in the chamber where the temperature variation is violent. Droplets whose size fall into a certain range are in favour of combustion efficiency. Thus efficient combustion requires a deep understanding of the droplet dynamics with temperature effects.

(a) Glockner and Naterer (2005)   (b) Darhuber et al. (2003)
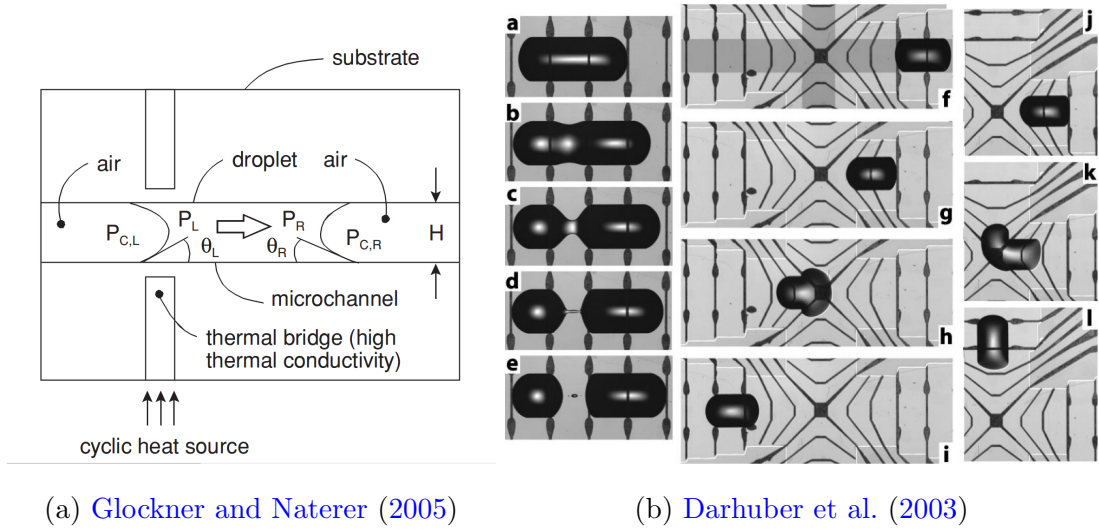
Figure 1.2: Examples of microfluidic actuation by thermocapillary stress: (a) thermocapillary pumping in a closed micro-channel; (b) micro-droplet splitting, propulsion and a 90° turn under thermocapillary stress.

Microfluidic devices which can simultaneously propel different liquids through individually addressable channels have attracted considerable attention, as parallel operation accelerates automated synthesis and analysis of small liquid samples (Yi et al., 2003). Thermocapillary stress arising from the temperature variation can be used to manipulate the motion of the micro-droplet (Darhuber et al., 2003), as illustrated in Figure 1.2.

The motivation of this study is to investigate the role temperature plays in non-isothermal multiphase flows with a numerical approach. The whole flow system in industrial application is highly intractable, as it may involve numerous droplets. However, it can be idealised into simple problems which can be handled, for instance, slender liquid jet breakup, droplet collision, droplet impact

3

and droplet migration on solid surface (all in non-isothermal situation). The study looks at small scales, where surface tension is usually dominant. Investigating these problems can shed new insights on the fundamental mechanisms and can also give hints on understanding industrial processes where non-isothermal multiphase flow is involved.

1.2 Literature Review

The review focuses on thermocapillary flow, as at small scales surface tension is dominant. The surface tension σ characterises macroscopically the molecular interactions that occur on the interface between two immiscible fluids. It leads to the discontinuity of stress tensor on the interface:

$$\left[\mathbf{n} \cdot \left(-p\mathbf{I} + \mu\left((\nabla\mathbf{u}) + (\nabla\mathbf{u})^T\right)\right)\right]_{-}^{+} = \sigma\kappa\mathbf{n} - \nabla\sigma, \tag{1.1}$$

in which $\mathbf{n}$ is the normal vector and κ the curvature.

When the fluids are subject to an externally imposed temperature difference ΔT, surface tension gradients are induced and shear stress (Marangoni stress) arises. The shear stress causes fluid motion on the interface and eventually leads to the flow in the bulk fluid. This is called thermocapillary flow.

The coupling between heat transfer and fluid motion, together with the moving interface boundary make it hard to study thermocapillary flow. Efforts have been made to the study of thermocapillary instabilities before the development of computing facilities enables researchers to investigate the dynamics with direct numerical simulation (DNS). Therefore the review is going to cover the study on thermocapillary instabilities and non-isothermal droplet dynamics. It is also necessary to discuss different numerical approaches as numerical simulation is the main approach in the study.

1.2.1 Thermocapillary Instabilities

The simplest example is a thin horizontal layer of a single fluid with a thickness of d and the surface is exposed to the passive gas, as sketched in Figure 1.3.
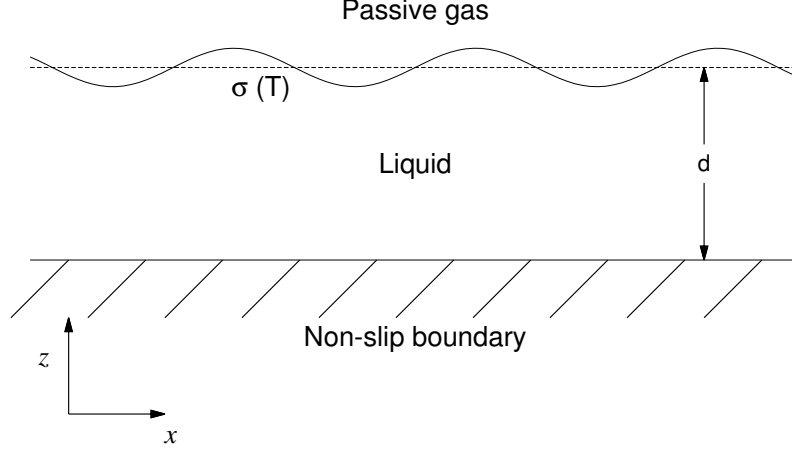
Figure 1.3: Sketch of One-Layer System

The liquid is a Newtonian fluid with reference density ρ_0, viscosity μ_0, thermal conductivity k, specific heat capacity c_p and volume expansion coefficient α; $\kappa = k/\rho_0 c_p$ is the thermal diffusivity and $\nu_0 = \mu_0/\rho_0$ is the kinematic viscosity. On the interface, the reference surface tension is σ_0 and h is the unit thermal surface conductance. The temperature of the passive air is a constant. The temperature dependence of surface tension and density is shown as (viscosity variation not considered):

$$\rho = \rho_0 - \alpha(T - T_0), \tag{1.2a}$$

$$\sigma = \sigma_0 - \beta(T - T_0). \tag{1.2b}$$

The liquid layer is subject to gravity g and a temperature gradient $\mathbf{b} = b_x \mathbf{e}_x + b_z \mathbf{e}_z$. Depending on the direction of the imposed temperature gradient, thermocapillary instabilities can be categorised into Marangoni-convection instability (perpendicular, $b_x = 0$) and thermocapillary-convection instability (parallel, $b_z = 0$). The strength of thermocapillarity, buoyancy effects driven by temperature difference and the ratio of viscous diffusion and thermal diffusion are characterised by Marangoni number Ma, Rayleigh number Ra and Prandtl number Pr, respectively. Crispation number C is used to study convection currents. C equals

to the product of a fluid's thermal diffusivity and dynamic viscosity divided by its undisturbed surface tension and a layer thickness. Thus, when $C \to 0$, interface deformation is negligible. Surface Biot number Bi represents the heat transfer between liquid and gas at the interface. The governing equations are Navier-Stokes equations with Boussinesq approximation and heat transfer equation. The following review is in non-dimensionalised form. For details of non-dimensionalisation and governing equations, the reader is referred to the work of Davis (1987).

$$Ma = \frac{\beta b d^2}{\rho_0 \nu \kappa}, \tag{1.3a}$$

$$Ra = \frac{\alpha g b_z d^4}{\nu \kappa}, \tag{1.3b}$$

$$Pr = \frac{\nu}{\kappa}, \tag{1.3c}$$

$$C = \frac{\mu \kappa}{d \sigma_0}, \tag{1.3d}$$

$$Bi = \frac{hd}{k}. \tag{1.3e}$$

When the liquid layer is heated from below ($b_x = 0$), Bénard (1901) observed the hexagonal convection in a layer of spermaceti, in which the flow is upwards under the surface depressions and downwards under surface elevation. He measured the wave number of the convection ($k \approx 2.2$). The cause of the convection is attributed to buoyancy by Rayleigh (1916). However, thermocapillarity also contributes to the convection and it is the dominant mechanism when the layer is thin. Pearson (1958) explained the mechanism with thermocapillarity. He applied linear instability theory to find the neutral condition corresponding to the onset of the steady convection. The basic state corresponds to static fluid, purely conductive heat transfer and hydrostatic pressure. In his study, the interface was treated nondeformable ($C \to 0$) and gravity was negligible ($Ra = 0$). The critical Marangoni number and overall wave number for a fixed temperature lower plate ($Ma_c \approx 79.6$, $k_c \approx 1.99$) and for a fixed heat-flux plate ($Ma_c \approx 48$, $k_c \to 0$) were identified. These two situations were later called short-wavelength mode and long-wavelength mode. Further, the rise of Bi results in the rise of Ma, leading to a conclusion that heat loss to passive air results in a stabilisation of the basic state.

Similar studies were carried out on the coupled thermocapillarity/buoyancy instability problem with nondeformable interface by Nield (1964) and Neild's model predicted well the experimental conditions for the onset of convection in shallow layers (Hoard et al., 1970). In order to include interface deflection, Davis (1983) derived a one-layer model nonlinear evolution equation for long-wave instability and obtained $Ma_c = 2G/3$, in which $G = gd^3/\nu\kappa$ is the Galileo number. This result was later confirmed by the silicone oil experiment conducted by Vanhook et al. (1997). Energy stability theory was utilized to obtain the criterion for stability by Davis (1969) on a Nield model with nondeformable interface. The post-instability behaviour can be examined by nonlinear analysis (Cloot and Lebon, 1984; Scanlon and Segel, 1967; Vanhook et al., 1997)

When the imposed temperature gradient is parallel to the liquid layer interface ($b_z = 0$), thermocapillary-convection instabilities arises. There are two basic states, the linear-flow basic state for an open system and the return-flow basic state for a closed system (Smith and Davis, 1983a). In addition, Smith and Davis (1983a,b) have identified two distinct classes of instabilities associated with the two basic states, namely the convective instabilities and the surface-wave instabilities. The mechanism of convective instabilities involves a balance between heat conduction and heat convection at the free surface and therefore the instabilities do not depend on surface deformation strongly, while the mechanism of the second class involves the mechanical transfer of momentum from the basic state to the disturbances and are highly dependent on the surface deformation. Linear theory was applied to study these instabilities and critical Ma versus Pr were examined for two basic states in the limit $Bi \to 0$. They predicted the regions for steady cellular structures and oscillatory states as well as the transition from a steady, unicellular basic state to an oscillatory state in the form of hydrothermal waves. The predicted transition was verified in later experimental work (Riley and Neitzel, 1998; Villers and Platten, 1992). Smith (1986) explained the physical mechanisms of these instabilities and nonlinear analysis was carried out by Smith (1988).

In addition to match with theoretical prediction, experimental work on thermocapillary instabilities identified secondary instability and celluar patterns evolution in Marangoni instabilities ($b_x = 0$) and multicellular transition in hy-

drothermal instabilities ($b_z = 0$). Details of experimental work are summarised by Schatz and Neitzel (2001) and analysis techniques are reviewed by Cross and Hohenberg (1993).

1.2.2 Axisymmetric Thermocapillary Instabilities and Non-Isothermal Droplet Dynamics

Extensive research has been carried out on thermocapillarity with the simplest geometry of an infinite liquid layer. If the no-slip boundary in Figure 1.3 is replaced by an axisymmetric axis, the problem is transformed into a slender jet and if no-slip boundaries are imposed on the two ends of the liquid, a liquid bridge is attained. For the liquid jet and the liquid bridge in isothermal situation, the instability, breakup dynamics and post-breakup behaviours are studied extensively and are reviewed by Eggers (1997).

Xu and Davis (1983, 1984) employed lubrication theory to study liquid bridge subject to an axial temperature gradients and obtained a class of similarity solutions, valid in the core region away from the endwalls of the bridge. Bauer (1984) provided the first linear study on the instability of an infinitely long axisymmetric liquid jet with thermocapillarity. He assumed a Stokes flow, imposed an arbitrary axially periodic temperature field on the liquid surface and obtained an analytical solution for the growth rate of the disturbance. It was concluded that the breakup of a liquid jet may not only occur for surface amplitude disturbances with wavelengths larger than the circumference of the jet (result from isothermal jet instability), but also takes place through oscillatory temperature gradients which excite the calm free surface. Xu and Davis (1985) considered a linear temperature gradient along the liquid surface. Lubrication theory gave the velocity and temperature distributions inside the jet due to a convective heat transfer with the ambient. They found that the capillary instabilities can be greatly retarded and even suppressed by surface wave instabilities.

In a nonlinear analysis by Mashayek and Ashgriz (1995) on liquid jets with thermocapillarity, they considered two different disturbances: thermal disturbance in the ambient and on the surface. In the first case, thermocapillary flow

is induced by ambient thermal disturbance and capillary flows can be made in opposite directions so that they cancel each other. In the second case, a small temperature disturbance on the interface can quickly induce a surface disturbance, leading to the breakup. The former explained why there was no significant effect on the breakup when a thermal disturbance was applied on the jet at the nozzle in the experiment of Faidley and Panton (1990). Pillai et al. (2012) applied the one-dimensional slender jet approximation on the governing equations. They identified a shorter breakup length. Compared with the experiments conducted with Wood's metal, their nonliner analysis failed to predict secondary breakup, which forms satellite droplets.

A great deal of research work has been conducted on droplet dynamics due to the importance of droplet in industrial application. Similarly, plentiful work has been carried out on isothermal droplet dynamics, including droplet impact, droplet collision and droplet spreading. This review focuses on non-isothermal situation according to our specific research interest.

The simplest example of non-isothermal droplet dynamics is droplet migration in another fluid due to temperature gradients. Young et al. (1959) were the first to analyse the thermocapillary migration of droplets. Considering Stokes flow, they calculated the terminal velocity of migration of a droplet placed in an infinite fluid, with a linear temperature distribution far away from the droplet. Experimental work was performed on the bubble migration in a liquid and good agreement with the theoretical analysis was achieved. The assumptions made were relaxed in subsequent work. For instance, Thompson et al. (1980) considered the inertia and convection of energy included and Haj-Hariri et al. (1997) included droplet deformation. Details in droplet/bubble migration driven by thermocapillarity can be found in the review of Herrmann et al. (2008).

The behaviour of a singe droplet subject to a temperature gradient is reasonably well understood: the terminal velocity of a droplet first decrease with increasing Ma, attains a minimum and then increases with a further increase of Ma; the droplet deforms oblate or prolate depending on the density ratio with the surrounding fluid (Nas and Tryggvason, 2003). Thus recently research focus has switched to multiple droplet interaction. Meyyappan et al. (1983) investigated analytically the motion of two non-deformable bubbles with the same size,

moving along their lines of centre. The terminal velocity of two bubbles were obtained in the limit of zero Re and Ma. The research was later generalised to arbitrarily oriented bubbles (Meyyappan and Subramanian, 1984). Anderson (1985) examined analytically the motion of two liquid drops oriented arbitrarily subject to a temperature gradient. He identified the effects of viscosity, thermal conductivity, size ratio and the distance between drops on the terminal velocity. Keh and Chen (1993) investigated analytically the axisymmetric thermocapillary motion of two spherical droplets moving along their line of centres in a Stokes flow. These assumptions of vanishing Ma and Re were relaxed in DNS and further studies were carried out on the influence of various non-dimensional number (Nas and Tryggvason, 2003; Yin and Li, 2015). It is worthwhile to mention that in the above research on non-isothermal droplet collision, only non-merging situation (low Re) were considered, while a few literature documented non-isothermal droplet coalescence. The suppression of droplet coalescence by temperature gradients was reported in the experimental work of Dell'Aversana et al. (1996) and further research is needed for the study on droplet collision with a higher Re.

In droplet dynamics associated with a substrate, the contact angle has to be taken into consideration, as three phases, liquid, gas and solid, are involved. Ehrhard and Davis (1991) studied the droplet spreading on a horizontal plate, which is uniformly heated or cooled. Under such heating, a vertical temperature gradient is established within the drop. They applied the lubrication approximation to simplify Navier-Stokes equations and derived a general evolution equation for the droplet height. This equation was solved in the limit of vanishing Crispation number (1.3e). In their solution, the droplet undergoes a quasi-static spreading as the motion is controlled by a constitutive law which relates the contact angle to the contact-line speed. By comparing the process of isothermal and non-isothermal spreading, they drew the conclusion that the heating plates retards spreading while cooling plates augments spreading. Ehrhard (1993) performed experiments on an axisymmetric isothermal and non-isothermal droplet spreading and confirmed the effects of heating/cooling plates on droplet spreading.

Bostwick (2013) considered the non-isothermal spreading of a droplet on a differentially heated substrate instead of uniformly heated. Both vertical and radial temperature gradients along the droplet interface are generated under such

non-uniformly heating. They also used the lubrication approximation for simplicity and identified the effects of interaction between temperature gradients in two directions on the quasi-static spreading. Sui and Spelt (2015) studied non-isothermal spreading on uniformly heating substrate, but they modified the lubrication theory for slip-limited spreading. Further DNS results showed that the thermal effects can reverse for large contact angle or large viscosity of outer fluid: spreading is inhibited by a cold plate and promoted by a hot plate. When a droplet attached on a non-isothermal heated solid wall, droplet migrations occur. Similar to droplet spreading, the contact angle also plays an important role in droplet migration. The experimental work of Yarin et al. (2002) using droplets on glass fibres and copper wires showed that the droplet moves towards the cold side, while in 2D DNS of droplet migration for a large contact angle there exists a regime where the droplet moves towards the hot side (Sui, 2014).

When the temperature variation is sufficiently violent, evaporation plays an important role in non-isothermal dynamics. An example is Leidenfrost effect which describes the phenomena of droplet held up by layer of vapour on a heated surface. For further details, the reader is referred to the review by Quéré (2013) and this study will not include evaporation effect.

1.2.3 Interface Tracking Methods and Spurious Currents

Rapid development of computational power has made direct numerical simulation (DNS) an important approach in fluid dynamics. The term DNS is used to refer to simulations of complex unsteady flow, where the governing equations (Navier-Stokes equations) are solved using suffciently fine grids so that all continuum time and length scales are sufficiently resolved without any hypothesis beyond continuum assumption (Prosperetti and Tryggvason, 2007). Therefore, DNS offers more detatiled and accurate flow field than analytical approach and can deal with flows which it is hard to conduct experiments to model.

As indicated before, the shape, location and evolution of the interface cause considerable difficulties in multiphase flows and hence, interface tracking is one major task in DNS of mulitphase flows. The problems involved are: (a) how to represent interface on a finite mesh? (b) how to describe the evolution of

the interface? (c) how to apply boundary conditions (discontinuities of fluid properties and surface tension) on the interface?

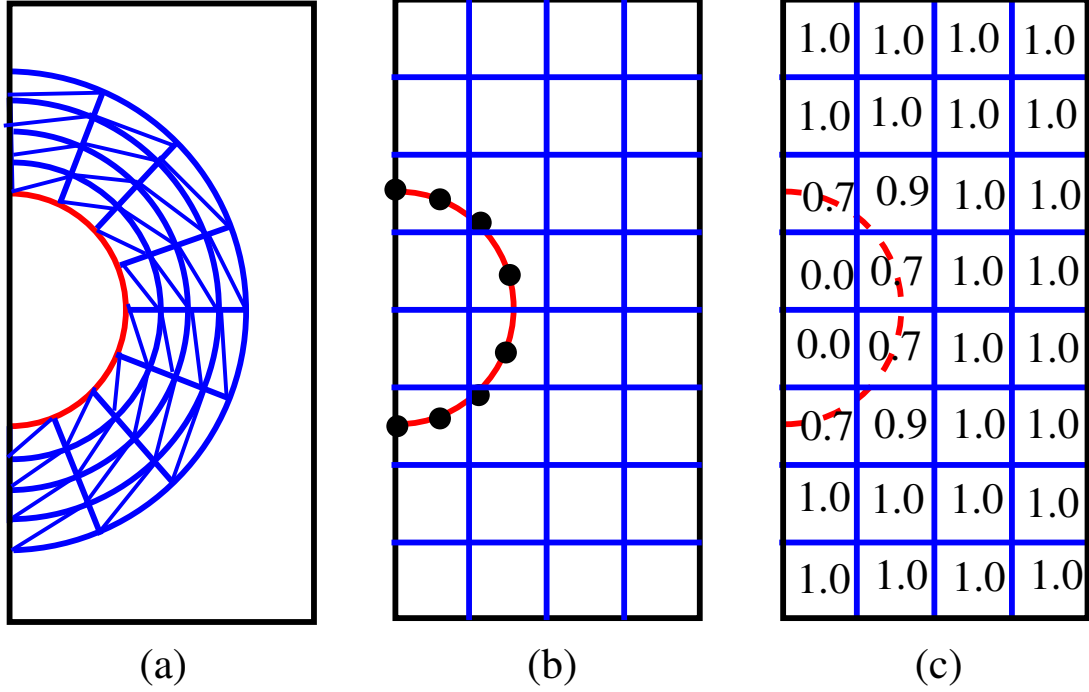| 1.0 | 1.0 | 1.0 | 1.0 |
1.0	1.0	1.0	1.0
0.7	0.9	1.0	1.0
0.0	0.7	1.0	1.0
0.0	0.7	1.0	1.0
0.7	0.9	1.0	1.0
1.0	1.0	1.0	1.0
1.0	1.0	1.0	1.0

(a)   (b)   (c)

Figure 1.4: Comparison of different interface-tracking methods representing a circular bubble: (a) the interface is a line of the moving mesh; (b) the interface is represented by a set of marker points located on the itnerface; (c) the interface captured by a volume fraction function

Various interface tracking methods have been developed to solve the three problems. These can be classified into two main categories: Lagrangian method with a moving mesh and Eulerian method with a fixed mesh. In Eulerian method, the interface is represented implicitly through a colour function, while in Lagrangian method, the interface is represented expliciyly by a line of mesh edge. Front-tracking can be described as a hybrid between the two methods as the Lagrangian marker points on the interface are used for explicitly tracking on a fixed mesh.

Eulerian method uses a single set of governing equation for the whole flow field. Density and viscosity are functions of the colour funciton value. The surface

tension is treated using a continuous surface force (CSF) model (Brackbill et al., 1992), in which surface tension is interpreted as a continuous force across the interface rather than a boundary value condition. Volume of Fluid (VOF), level-set and diffuse interface method fall into this category.

In Lagrangian method, the interface is represented by a line of mesh explicitly. One of the distinct features of this type of method is that the mesh moves with the interface in order to always fit the interface. A direct consequence is the accurate representaion of the interface and neat interpretation of interfacial boundary condition. Hirt et al. (1974) firstly put forward an arbitrary Lagrangian-Eulerian (ALE) computing method for fluid flow, in which the mesh may move with fluid (Lagrangian), or keep fixed (Eulerian). When ALE is applied in multiphase flow, the interfacial mesh is moving with the evolution of the interface and the interior mesh stays fixed. This ensures accurate track of the interface and avoids considerable distortion of the whole mesh.

The advantages of Eulerian methods are that (Scardovelli and Zaleski, 1999): (a) they are easy to realise on a Cartesian mesh; (b) they can be easily extended to three-dimension; (b) they can handle topology changes easily without special provision to perform reconnection or breakup of the interface. But unphysically topology change may take place or take place in advance if the grid is not sufficienty fine to resolve thin region between two interfaces. Lagrangian methods can track the interface much more accurately and the unphysically merge and breakup of the interface can be avoided. As the mesh is not fixed, it is also easy to perform adaptive mesh refinement to reduce computing cost (Quan, 2011). Therefore, Lagrangian method is more accurate for multiphase flows with moderate deformation of the interface.

Regardless of the method adpoted to track the interface, DNS of multiphase flows suffers from spurious current (parasitic velocity), especially when surface tension is the dominant physical mechanism. The characters of spurious current include lack of convergence with spatial refinement or convergence to a solution different from the exact solution. It has been reported in the practice of various interface tracking methods (Popinet and Zaleski, 1999; Renardy and Renardy, 2002; Tryggvason et al., 2001). A typical example is the numerical solution of a stationary cicular bubble.
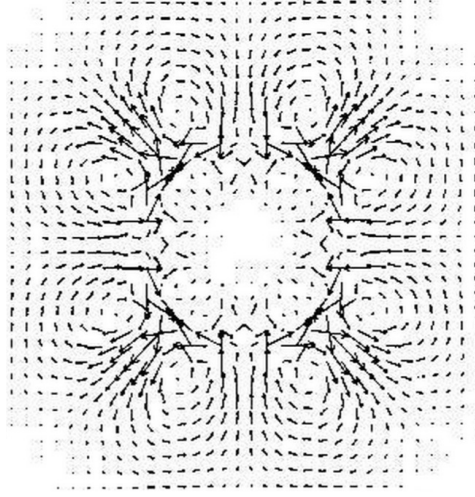
Figure 1.5: Spurious currents around a stationary bubble. (Simulation using VOF by Popinet and Zaleski (1999))

The analytical solution corresponds to zero velocity and constant pressure in each fluid but with a pressure jump across the interface. However, numerical simulation is illustrated in Figure 1.5 and spatial refinement can not eliminate the parasitic velocity. Spurious current can cause serious results in multiphase flow simulation as it generates unphysical movement of the interface.

Gerbeau et al. (1998) pointed out that the non-physical velocity is inevitable when the incompressible fluid is subjected to external forces and surface tension is viewed as a local external force. They explained that the numerical velocity is not rigorously divergence-free (the incompressible constraint). Ganesan et al. (2007) identified the other sources for spurious current in multiphase flow: the approximation of the unknown interface and of the curvature in capillary forces.

Although spurious current will not vanish with spatial refinement, various approaches have been proposed to reduce it, mainly through better fit of the interface and more accurate calculation of curvature. Popinet and Zaleski (1999) introduced a correction in pressure to solve the inconsistent modelling of surface tension in marker and cell (MAC) staggered grid. Cubic spline was employed to construct a more accurate interface in their front-tracking method. Renardy and Renardy (2002) replaced the linear segment interface construction algorithm

in their VOF method and proposed parabolic reconstruction of surface tension (PROST) to determine better interface geometric characters through optimal fitting. Besides, a higher order interface advection scheme and an improved projection method are proposed. Ganesan et al. (2007) examined the performance of discontinuous pressure and isoparametric finite element in their ALE approach. In their isoparametric finite element approach, the interface using second-order curved edge rather than straight edge. Their results showed that using discontinuous pressure approximations and isoparametric finite elements can greatly reduce spurious currents.

In multiphase flows with temperature effects, the spurious current can lead to disatrous results. DNS of non-isothermal multiphase flow has a higher demand for interface representation compared with isothermal simulation: the induced surface tension gradient and the arising Marangoni stress are along the interface. Spurious current results in unphysical evolution of the interface and hence inaccuracy in both direction and magnitude of surface tension gradient and Marangoni stress. This local inaccuracy will then unphysically change the temperature field and velocity field near the interface and eventually the whole computing domain as surface tension is the dominant force in the problems we study. Therefore, a method with reduced spurious currents is necessary for the numerical study of multiphase flow with temperature effects.

1.3 Present Work

Multiphase flow problems are highly intractable due to the existence of the unknown boundaries and the temperature variation makes it even more complicated. Extensive research work has been carried out on thermocapillary instabilities with the simplest geometry, a liquid layer. Various mechanisms of how an imposed temperature gradient drives the flow have been identified from the work on a liquid layer and these are utilised in the study of thermocapillary instabilities in a different geometry: liquid bridge and liquid jet. With the rapid development of high performance computing facilities, the non-isothermal droplet dynamics,

including single droplet migration, droplet collision and droplet spreading, can be dealt with through DNS.

Motivated by the technical applications including inkjet printing, atomisation and droplet actuation, we focuses on droplet dynamics and capillary jet breakup with temperature effects. Previous studies of thermocapillary instabilities have obtained a great deal of results, both theoretical and experimental. However, linear and nonlinear analysis make too many assumptions, for instance nondeformable interface, lubrication approximation and one-dimensional slender jet approximation. These assumptions limit the application of the solution. Experimental work also has its obstacles, for example difficulties in setting temperature conditions, measuring temperature and differentiating the effects of thermocapillarity from those of gravity. Direct numerical simulation is a sound approach as least assumptions are made in DNS and detailed flow field information is provided. Various interface tracking methods have also been developed to handle the most difficult part, the moving interface. However DNS suffers a lot from spurious currents, which can cause catastrophic results, especially for non-isothermal multiphase flow which has a higher demand for interface accuracy. Our current method is a finite element ALE method on the triangular mesh with straight edges. As illustrated in Figure 1.6, the interface (blue solid line) is represented by a group of piecewise line segments (red solid line) in our method. The deviation of the calculated tangent direction from the analytical one is huge, and especially for a vertex node, there are two tangent directions as it is a common node for two edges. This leads to the inaccuracy in Marangoni stress calculation.

There are two main parts in the study: to develop an accurate method for non-isothermal multiphase flows and to employ this method to study capillary jet breakup and droplet dynamics with thermocapillarity. In the first part, heat transfer equations and Navier-Stokes equations are solved together and isoparametric (with curved edge) finite element method is utilised for better representation of the interface and for reduction of spurious currents. The problems we intend to study can be idealised into a simple geometry: two-dimensional or axisymmetric. Hence we are going to develop the numerical method for these two geometries. As the method is general, it can be applied to study various types
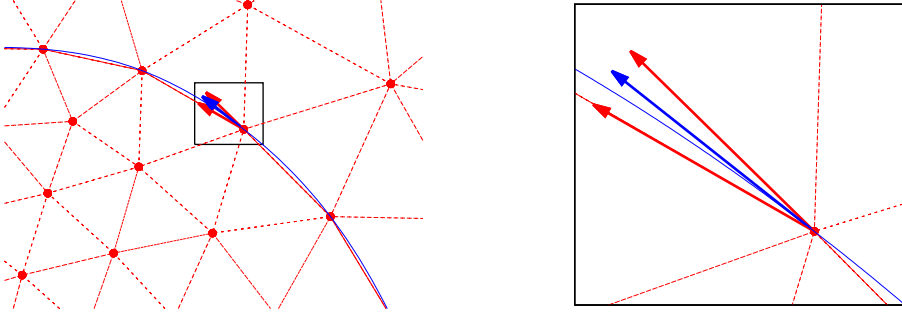
Figure 1.6: Comparison of the calculated tangent directions and the analytical direction on a vertex node.

of multiphase flows in these two geometries. The well-studied problems, including thermocapillary instabilities of a liquid layer and single droplet migration with imposed temperature gradients, can be used as validation for our numerical method. The second part of the study is to apply our method on jet breakup and droplet dynamics with thermocapillarities. The problems we are currently interested in are the temperature effects in the satellite droplet formation in jet breakup, droplet collision with relatively higher Re number and droplet spreading with higher contact angle.

The rest of the report is as followed: Chapter 2 introduces numerical method which is employed in the current study, including the theory of finite element method, Navier-Stokes solver, mesh generator and interface representation; Chapter 3 presents the development made on the numerical method, the coupling of flow solver with heat transfer equation and isoparametric methods included; Chapter 4 shows the validation for the numerical development; Chapter 5 summarises the work documented in this report; Chapter 6 lists a programme of the future study, including the estimated of timing and dates.

Chapter 2

Numerical Method

2.1 Finite Element Method

2.1.1 Theory

The finite element method (FEM) is a flexible and powerful technique for finding approximate solutions to partial differential equations. The method is based on the idea that the solution of differential equations can be approximated by a linear combination of appropriately selected function ϕ_i, which are called basis function, in the entire domain of the problem. For elementary introductions to the finite element method, the reader is advised to see Gockenbach (2006).

A boundary value problem (BVP) can be transformed into the weak formulation. The weak formulation is obtained by multiplying a function on both sides of the equation and then integrating over the whole domain. The weak formulation can be transferred into algebraic equations through discretisation. Hence the BVP can be solved numerically.

The method is best illustrated with an example of solving a Poisson equation

in a two-dimensional space:

$$-\nabla \cdot (k\nabla u) = f \quad \text{in} \quad \Omega, \tag{2.1a}$$

$$u = g \quad \text{on} \quad \partial\Omega_1, \tag{2.1b}$$

$$\partial u/\partial n = h \quad \text{on} \quad \partial\Omega_2. \tag{2.1c}$$

where u, f, k, g, h are scalar functions, Ω is a bounded open domain, $\partial\Omega_1$ is the Dirichlet boundary and $\partial\Omega_2$ is a Neumann boundary.

Multiply (2.1a) with a test function v and integrate it over the whole domain to obtain the weak formulation:

$$\int_\Omega -\nabla \cdot (k\nabla u)v d\Omega = \int_\Omega fv d\Omega. \tag{2.2}$$

Then use the product rule on the left hand side:

$$\int_\Omega (-\nabla \cdot (kv\nabla u) + k\nabla u \cdot \nabla v)d\Omega = \int_\Omega fv d\Omega. \tag{2.3}$$

It is essential to apply Green's first identity onto the first term of the left hand side:

$$\int_{\partial\Omega} -kv\frac{\partial u}{\partial n}dl + \int_\Omega k\nabla u \cdot \nabla v d\Omega = \int_\Omega fv d\Omega. \tag{2.4}$$

The whole domain is discretised into triangular mesh (Figure 2.1). In each element, the solution u is approximated as:

$$u = \sum_{i=0}^{N} u_i \phi_i(x, y), \tag{2.5}$$

in which u_i is the solution on the node (x_i, y_i) and $\phi_i(x, y)$ satisfies

$$\phi_i(x_j, y_j) = \begin{cases} 1 & i = j \\ 0 & i \neq j \end{cases}. \tag{2.6}$$

The key idea of Galerkin finite element method is to use the basis functions as test functions. This results in a system of N equations (N is the number of nodes), i.e., i takes value from 1 to N:
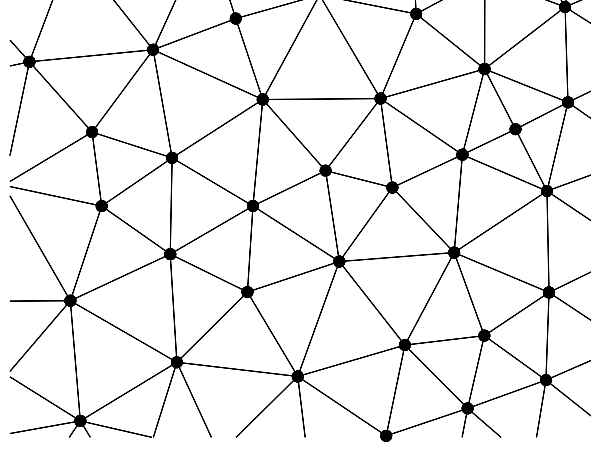
Figure 2.1: Finite element triangulation

$$\sum_{j=1}^{N}(\int_{\Omega} k\nabla\phi_i \cdot \nabla\phi_j)u_j = \sum_{j=1}^{N}\int_{\Omega}\phi_i\phi_j d\Omega f_j + \int_{\partial\Omega} k\phi_i \frac{\partial u}{\partial n}dl, \tag{2.7}$$

which can be expressed as a matrix problem:

$$\mathbf{A}^k\mathbf{u}^k = \mathbf{M}^k\mathbf{f}^k + \mathbf{g}^k. \tag{2.8}$$

$\mathbf{A}^k$ is called the stiffness matrix and $\mathbf{M}^k$ is called the mass matrix. $\mathbf{u}^k = (u_0, ..., u_N)^T$ is the solution vector and $\mathbf{f}^k = (f_0, ..., f_N)^T$ is related to the right hand side of the Poisson equation. The vector $\mathbf{g}_k$ is associated with the Neumann boundary condition. Solving (2.8) we can get the approximation on each node.

Equation (2.8) is only for one element. In practise, the stiffness matrix is built by summing up the contributions of all triangles in the domain, by apply the formula:

$$A_{ij} = \sum_{k=1}^{K} A_k(i,j), \tag{2.9}$$

in which K is the number of triangles containing node i and node j and $A_k(i,j)$ is an integration over triangle k (Ω_k notes the triangle k and ϕ^k notes the basis function in triangle k).

$$A_k(i,j) = \int_{\Omega_k} k\nabla\phi_i^k\nabla\phi_j^k d\Omega. \tag{2.10}$$

Now look at the term $\int_{\partial\Omega} k\phi_i \partial u/\partial n \, dl$ the right hand side of (2.7). $\partial\Omega$ means the element boundary, which is the three edges of a triangle. If one edge is an interior edge in the whole domain, there will be two triangles containing it. Although the $\partial u/\partial n$ is unknown, the integrations along the edge of the two triangles containing this edge cancel each other. If the edge is an edge on the boundary with Neumann boundary condition $\partial u/\partial n = h$, it can be written as $\int_{\partial\Omega} k\phi_i h \, dl$, which is a known term. The nodes on a Dirichlet boundary have known solutions and they can be excluded from the solution vector by adding corresponding terms on the right hand side vector, which is called the load vector.

Hence the Poisson equation (2.1) can be transferred to a system of linear algebraic equations which can be solved by computers:

$$\sum_{\substack{i=1,\dots,N \\ j=1,\dots,N}}^{i,j\in\mathbf{U}} A_{ij}u_i = \sum_{j=1,\dots,N}^{j\in\mathbf{U}} (f_j + g_j), \tag{2.11}$$

where $\mathbf{U}$ is the set of the number of node with unknown value.

2.1.2 Implementation

Having studied the theory of finite element method, the next step is to implement these method numerically. One important part of the implementation is to obtain the basis functions before assembling the stiffness matrix and load vector.

P1 finite element method uses the simplest linear functions of the form: $a + bx + cy$ as basis functions. The basis functions are defined at three vertices (Figure 2.2a).

The basis functions $\varphi_i(s,t)$ for each node defined in the reference triangle below are:

$$\varphi_0(s,t) = 1 - s - t, \tag{2.12a}$$
$$\varphi_1(s,t) = s, \tag{2.12b}$$
$$\varphi_2(s,t) = t. \tag{2.12c}$$

The P2 finite element uses quadratic functions of the form: $a + bx + cy + dxy + ex^2 + fy^2$ as basis functions. These basis functions are defined at three vertices

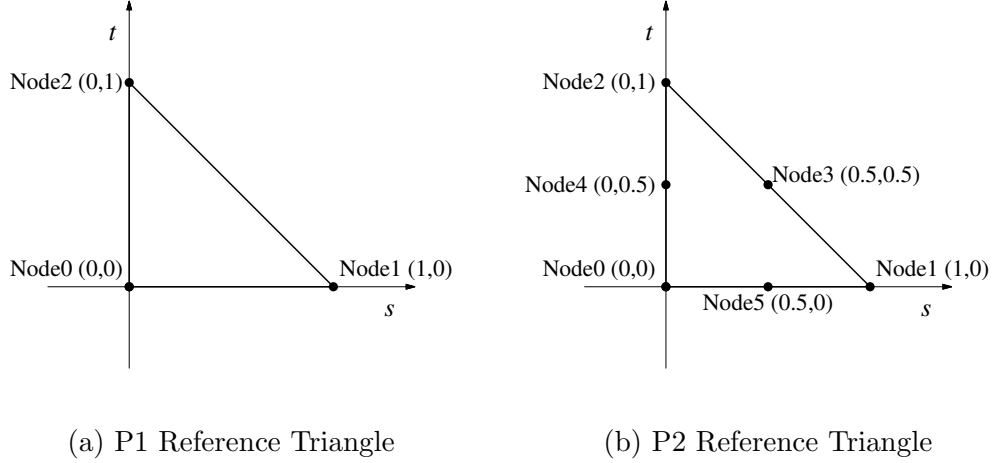(a) P1 Reference Triangle　　　　　　(b) P2 Reference Triangle

Figure 2.2: P1 and P2 referenced triangles in $s - t$ plane

and three edge midpoints (Figure 2.2b). The basis function $\varphi_i(s, t)$ for each node defined in the reference triangle below are:

$$\varphi_0(s, t) = (1 - s - t)(1 - 2s - 2t), \tag{2.13a}$$

$$\varphi_1(s, t) = s(2s - 1), \tag{2.13b}$$

$$\varphi_2(s, t) = t(2t - 1), \tag{2.13c}$$

$$\varphi_3(s, t) = 4st, \tag{2.13d}$$

$$\varphi_4(s, t) = 4t(1 - s - t), \tag{2.13e}$$

$$\varphi_5(s, t) = 4s(1 - s - t). \tag{2.13f}$$

With known basis functions, we can calculate the integrals $\int_\Omega \nabla\varphi_i \cdot \nabla\varphi_j d\Omega$ and assembly the stiff matrix or other forms of integrals for other matrices according to the need. The $\varphi_i(s, t)$ defined in the reference triangle need to be transformed to an arbitrary triangle geometry since elements have various directions and shapes in the domain. This transformation is illustrated in Figure 2.3.

The transformation from referenced triangle in $s - t$ plane to an arbitrary triangle in $x - y$ plane is an affine transformation ($\mathbf{J}$ is used to represent the
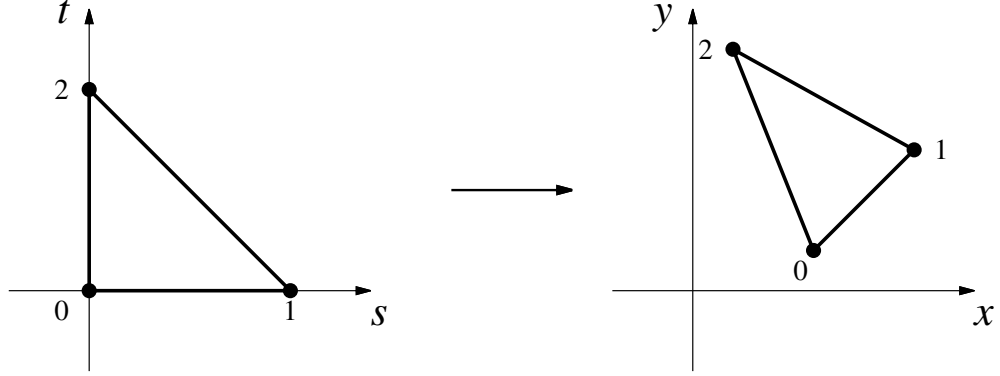
Figure 2.3: Transformation of a reference triangle to an arbitrary triangle

affine mapping):

$$\begin{pmatrix} x \\ y \end{pmatrix} = \begin{pmatrix} x_0 \\ y_0 \end{pmatrix} + \begin{pmatrix} x_1 - x_0 & x_2 - x_0 \\ y_1 - y_0 & y_2 - y_0 \end{pmatrix} \begin{pmatrix} s \\ t \end{pmatrix}, \tag{2.14a}$$

$$\mathbf{J} = \begin{pmatrix} \dfrac{\partial x}{\partial s} & \dfrac{\partial x}{\partial t} \\ \dfrac{\partial y}{\partial s} & \dfrac{\partial y}{\partial t} \end{pmatrix} = \begin{pmatrix} x_1 - x_0 & x_2 - x_0 \\ y_1 - y_0 & y_2 - y_0 \end{pmatrix}. \tag{2.14b}$$

Note that the transformed basis functions $\phi_i(x, y)$ are now defined in the $x - y$ plane. In this transformation, $\phi_i(x, y) = \varphi_i(s, t)$. By applying the inverse Jacobian matrix, $\partial \phi_i / \partial x$, $\partial \phi_i / \partial y$ can thus be calculated with the chain rule:

$$\nabla \phi_i = \begin{pmatrix} \dfrac{\partial \phi_i}{\partial x} \\ \dfrac{\partial \phi_i}{\partial y} \end{pmatrix} = \begin{pmatrix} \dfrac{\partial s}{\partial x} & \dfrac{\partial t}{\partial y} \\ \dfrac{\partial s}{\partial s} & \dfrac{\partial t}{\partial t} \end{pmatrix} \begin{pmatrix} \dfrac{\partial \varphi_i}{\partial s} \\ \dfrac{\partial \varphi_i}{\partial t} \end{pmatrix} = \mathbf{J}^{-\mathbf{T}} \cdot \nabla \varphi_i. \tag{2.15}$$

Hence, the integrals over an arbitrary triangle in $x - y$ plane are computed as:

$$\int_\Omega \nabla \phi_i \cdot \nabla \phi_j dx dy = \int_{\Omega_R} \left(\mathbf{J}^{-\mathbf{T}} \nabla \varphi_i \right) \cdot \left(\mathbf{J}^{-\mathbf{T}} \nabla \varphi_j \right) det(\mathbf{J}) ds dt. \tag{2.16}$$

in which Ω_R is the referenced triangle on $s - t$ plane. The use of referenced triangle simplifies the calculation of integrals over an arbitrary triangle.

2.2   Navier Stokes Solver

2.2.1   Mathematical Formulation

The governing equations for the flow is the Navier-Stokes equation. Since we deal with incompressible fluid, the incompressible constraint is included. The overall equations for incompressible flow in the coordinate-free vector notation are:

$$\rho\frac{d\mathbf{u}}{dt} = -\nabla p + \nabla \cdot \left[\mu\left((\nabla\mathbf{u}) + (\nabla\mathbf{u})^{\mathbf{T}}\right)\right] + \mathbf{f}, \tag{2.17a}$$

$$\nabla \cdot \mathbf{u} = 0. \tag{2.17b}$$

where $\dfrac{d}{dt}$ is the material derivative.

For two dimensional geometry, the equations turn into (2.18):

$$\rho\frac{du}{dt} = -\frac{\partial p}{\partial x} + \frac{\partial}{\partial x}\left(2\mu\frac{\partial u}{\partial x}\right) + \frac{\partial}{\partial z}\left(\mu\left(\frac{\partial u}{\partial z} + \frac{\partial v}{\partial x}\right)\right) + f_x, \tag{2.18a}$$

$$\rho\frac{dv}{dt} = -\frac{\partial p}{\partial z} + \frac{\partial}{\partial x}\left(\mu\left(\frac{\partial u}{\partial z} + \frac{\partial v}{\partial x}\right)\right) + \frac{\partial}{\partial z}\left(2\mu\frac{\partial v}{\partial z}\right) + f_z, \tag{2.18b}$$

$$\frac{\partial u}{\partial x} + \frac{\partial v}{\partial z} = 0. \tag{2.18c}$$

where velocity $\mathbf{u} = (u, v)$ is in $x - z$ plane.

For axisymmetric geometry, the equations turn into (2.19):

$$\rho\frac{du}{dt} = -\frac{\partial p}{\partial r} + \frac{1}{r}\frac{\partial}{\partial r}\left(r2\mu\frac{\partial u}{\partial r}\right) - \frac{2\mu u}{r^2} + \frac{\partial}{\partial z}\left(\mu\left(\frac{\partial u}{\partial z} + \frac{\partial v}{\partial r}\right)\right) + f_r, \tag{2.19a}$$

$$\rho\frac{dv}{dt} = -\frac{\partial p}{\partial z} + \frac{1}{r}\frac{\partial}{\partial r}\left(r\mu\left(\frac{\partial u}{\partial z} + \frac{\partial v}{\partial r}\right)\right) + \frac{\partial}{\partial z}\left(2\mu\frac{\partial v}{\partial z}\right) + f_z, \tag{2.19b}$$

$$\frac{1}{r}\frac{\partial}{\partial r}(ru) + \frac{\partial v}{\partial z} = 0. \tag{2.19c}$$

where velocity $\mathbf{u} = (u, v)$ is in $r - z$ plane and $r = 0$ is the axis of rotation.

2.2.2   Element

In the current study triangular elements are employed since they allow the greatest flexibility when dealing with arbitrary geometries. The intention of the
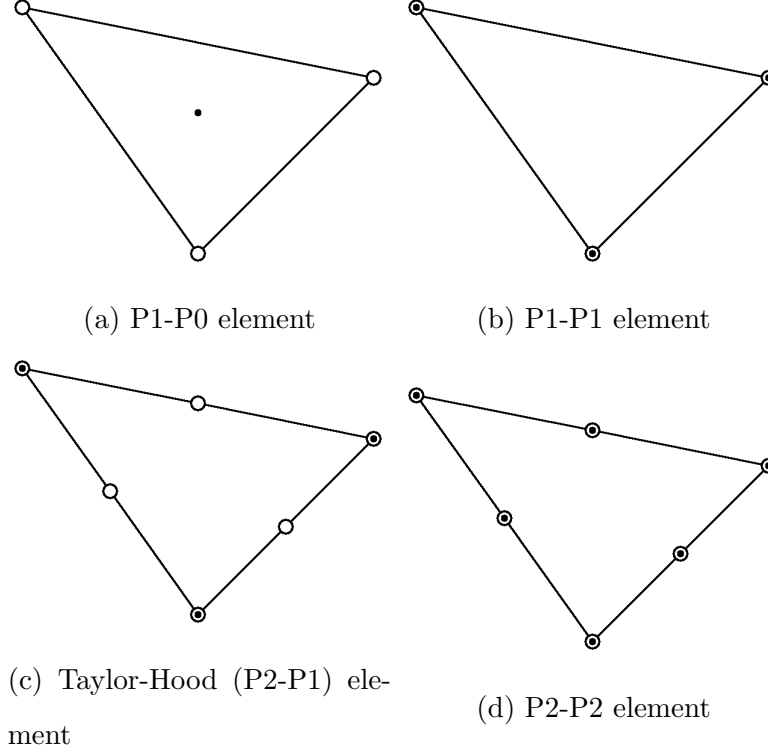
(a) P1-P0 element

(b) P1-P1 element

(c) Taylor-Hood (P2-P1) element

(d) P2-P2 element

Figure 2.4: Common elements for incompressible flows. ∘: velocity degree of freedom; •: pressure degree of freedom

study is to solve the Navier-Stokes equations, and thus an element is required that can be be used to interpolate both velocity and pressure fields. The elements in Figure 2.4 are all potentially useful for modelling incompressible flow. However, the elements in Figure 2.4a, b and d fail to satisfy Ladyzhenskaya-Babushka-Brezzi (LBB) stability condition (Gunzburger, 1989).

Therefore, Taylor-Hood element in Figure 2.4c with linear pressure field and quadratic velocity field is chosen as the triangular element in the study.

2.2.3 Weak Formulation

The weak formulation is obtained by multiplying the governing equations with a test functions, noted ϕ and ψ and integrating the equations over the whole flow field. The P2 basis function of velocity ϕ is multiplied on the motion equation and

the P1 basis function of pressure is multiplied on the continuity equation. In this section, we only discuss the two-dimensional geometry. The weak formulation in axisymmetric geometry can be obtained similarly. The difference is that $\int_\Omega d\Omega$ corresponds $\int_\Omega dxdz$ in 2D geometry and $\int_\Omega rdrdz$ in axisymmetric geometry.

The weak form for 2D geometry is as followed:

$$\int_\Omega \rho\phi\frac{du}{dt}dxdz = \int_\Omega \phi\frac{\partial}{\partial x}\left(2\mu\frac{\partial u}{\partial x}\right)dxdz + \int_\Omega \phi\frac{\partial}{\partial z}\left(\mu\left(\frac{\partial u}{\partial z}+\frac{\partial v}{\partial x}\right)\right)dxdz$$

$$+ \int_\Omega f_x\phi dxdz - \int_\Omega \phi\frac{\partial p}{\partial x}dxdz,$$

(2.20a)

$$\int_\Omega \rho\phi\frac{dv}{dt}dxdz = \int_\Omega \phi\frac{\partial}{\partial x}\left(\mu\left(\frac{\partial u}{\partial z}+\frac{\partial v}{\partial x}\right)\right)dxdz + \int_\Omega \phi\frac{\partial}{\partial z}\left(2\mu\frac{\partial v}{\partial z}\right)dxdz$$

$$+ \int_\Omega f_z\phi dxdz - \int_\Omega \phi\frac{\partial p}{\partial z}dxdz,$$

(2.20b)

$$\int_\Omega \psi\frac{\partial u}{\partial x}dxdz + \int_\Omega \psi\frac{\partial v}{\partial z}dxdz = 0.$$

(2.20c)

Employ product rule and Green's first identity on (2.20b) and (2.20c) to obtain:

$$\int_\Omega \left(\rho\phi\frac{du}{dt}+2\mu\frac{\partial\phi}{\partial x}\frac{\partial u}{\partial x}+\mu\frac{\partial\phi}{\partial z}\frac{\partial u}{\partial z}+\mu\frac{\partial\phi}{\partial z}\frac{\partial v}{\partial x}-p\frac{\partial\phi}{\partial x}\right)dxdz$$

(2.21a)

$$= \int_{\partial\Omega} \phi\left[\left(-p+2\mu\frac{\partial u}{\partial x}\right)n_x + \mu\left(\frac{\partial u}{\partial z}+\frac{\partial v}{\partial x}\right)n_z\right]dl + \int_\Omega f_x\phi dxdz,$$

$$\int_\Omega \left(\rho\phi\frac{dv}{dt}+\mu\frac{\partial\phi}{\partial x}\frac{\partial u}{\partial z}+\mu\frac{\partial\phi}{\partial x}\frac{\partial v}{\partial x}+2\mu\frac{\partial\phi}{\partial x}\frac{\partial v}{\partial z}-p\frac{\partial\phi}{\partial z}\right)dxdz$$

(2.21b)

$$= \int_{\partial\Omega} \phi\left[\mu\left(\frac{\partial u}{\partial z}+\frac{\partial v}{\partial x}\right)n_x + \left(-p+2\mu\frac{\partial v}{\partial z}\right)n_z\right]dl + \int_\Omega f_z\phi dxdz,$$

$$\int_\Omega \psi\frac{\partial u}{\partial x}dxdz + \int_\Omega \psi\frac{\partial v}{\partial z}dxdz = 0.$$

(2.21c)

where $\mathbf{n} = (n_x, n_z)$ is the normal vector on the boundary.

26

2.2.4 Discretisation

The discretisation is done on a Taylor-Hood element. The pressure is approximated by the pressure value on the vertices, while the velocity is approximated by the value on six nodes. ϕ is chosen to be a quadratic P2 basis function and ψ is a linear P1 basis function. For LBB condition, velocity is discretised using ϕ and pressure is discretised using ψ, as in (2.22)

$$u \approx \sum_{i=0}^{N_{P2}} u_i \phi_i, \ v \approx \sum_{i=0}^{N_{P2}} v_i \phi_i, \ p \approx \sum_{i=0}^{N_{P1}} p_i \psi_i. \tag{2.22}$$

Subtitle the approximation of (2.22) into 2D weak formulation (2.21) to form a discretised weak formulation of 2D:

$$\sum_{i=0}^{N_{P2}} \left(\int_{\Omega} \rho \phi_j \phi_i dx dz \right) \frac{du_i}{dt} + \sum_{i=0}^{N_{P2}} \left(\int_{\Omega} \mu \left(2\frac{\partial \phi_j}{\partial x}\frac{\partial \phi_i}{\partial x} + \frac{\partial \phi_j}{\partial z}\frac{\partial \phi_i}{\partial z} \right) dx dz \right) u_i \tag{2.23a}$$

$$+ \sum_{i=0}^{N_{P2}} \left(\int_{\Omega} \mu \frac{\partial \phi_j}{\partial z}\frac{\partial \phi_i}{\partial x} dx dz \right) v_i - \sum_{i=0}^{N_{P1}} \left(\int_{\Omega} \frac{\partial \phi_j}{\partial x}\psi_i dx dz \right) p_i = \int_{\partial \Omega} \phi_j g_x dl + \int_{\Omega} \phi_j f_x dx dz,$$

$$\sum_{i=0}^{N_{P2}} \left(\int_{\Omega} \rho \phi_j \phi_i dx dz \right) \frac{dv_i}{dt} + \sum_{i=0}^{N_{P2}} \left(\int_{\Omega} \mu \left(\frac{\partial \phi_j}{\partial x}\frac{\partial \phi_i}{\partial x} + 2\frac{\partial \phi_j}{\partial z}\frac{\partial \phi_i}{\partial z} \right) dx dz \right) v_i \tag{2.23b}$$

$$+ \sum_{i=0}^{N_{P2}} \left(\int_{\Omega} \mu \frac{\partial \phi_j}{\partial x}\frac{\partial \phi_j}{\partial z} dx dz \right) u_i - \sum_{i=0}^{N_{P1}} \left(\int_{\Omega} \frac{\partial \phi_j}{\partial z}\psi_i dx dz \right) p_i = \int_{\partial \Omega} \phi_j g_z dl + \int_{\Omega} \phi_j f_z dx dz,$$

$$\sum_{i=0}^{N_{P2}} \left(\int_{\Omega} \psi_j \frac{\partial \phi_i}{\partial x} dx dz \right) u_i + \sum_{i=0}^{N_{P2}} \left(\int_{\Omega} \psi_j \frac{\partial \phi_i}{\partial z} dx dz \right) v_i = 0, \tag{2.23c}$$

in which

$$g_x = \left(-p + 2\mu\frac{\partial u}{\partial x} \right) n_x + \mu \left(\frac{\partial u}{\partial z} + \frac{\partial v}{\partial x} \right) n_z, \tag{2.24a}$$

$$g_z = \mu \left(\frac{\partial u}{\partial z} + \frac{\partial v}{\partial x} \right) n_x + \left(-p + 2\mu\frac{\partial v}{\partial z} \right) n_z. \tag{2.24b}$$

The summation of the line integrals on the right hand side of these equations equals zero for nodes not on the interface and for nodes on the interface, it can

be replaced by line integrals associated with surface tension. Full details are demonstrated in Chapter 2.3.

The integrals in (2.23) can be formed as matrices, thus condensing the problem into the following form:

$$\mathbf{M}_x \frac{d\mathbf{u}}{dt} + \mathbf{K}_{xx}\mathbf{u} + \mathbf{K}_{xz}\mathbf{v} + \mathbf{B}_x\mathbf{p} = \mathbf{f}_x + \mathbf{g}_x, \tag{2.25a}$$

$$\mathbf{M}_y \frac{d\mathbf{v}}{dt} + \mathbf{K}_{zx}\mathbf{u} + \mathbf{K}_{zz}\mathbf{v} + \mathbf{B}_z\mathbf{p} = \mathbf{f}_z + \mathbf{g}_z, \tag{2.25b}$$

$$\mathbf{B}_x^{\mathbf{T}}\mathbf{u} + \mathbf{B}_z^{\mathbf{T}}\mathbf{v} = \mathbf{0}. \tag{2.25c}$$

2.2.5 Solution

The material derivative is simply discretised to create a time-marching scheme.

$$\frac{d\mathbf{u}}{dt} \approx \frac{\mathbf{u}^{n+1} - \mathbf{u}^n}{\Delta t} \, , \, \frac{d\mathbf{v}}{dt} \approx \frac{\mathbf{v}^{n+1} - \mathbf{v}^n}{\Delta t}. \tag{2.26}$$

$\mathbf{u}_i^{n+1}$ represents the velocity at time $t = (n + 1)\Delta t$ of a particle whose location is $\mathbf{x}_i$, a mesh node position. For correctly modelling the convective acceleration, the velocity of this particle at time $t = n\Delta t$, $\mathbf{u}_i^n$ is found by following the line of characteristic backwards through the flow for one time step. This method ensures that the acceleration obtained is correct for the particle rather than for a fixed position in the field.

The matrices in (2.25) can be combined for simplified notation.

$$\mathbf{M} = \frac{1}{\Delta t} \begin{pmatrix} \mathbf{M}_x & 0 \\ 0 & \mathbf{M}_z \end{pmatrix}, \tag{2.27}$$

$$\mathbf{K} = \begin{pmatrix} \mathbf{K}_{xx} & \mathbf{K}_{xz} \\ \mathbf{K}_{zx} & \mathbf{K}_{zz} \end{pmatrix}, \tag{2.28}$$

$$\mathbf{B} = \begin{pmatrix} \mathbf{B}_x \\ \mathbf{B}_z \end{pmatrix}, \tag{2.29}$$

$$\mathbf{b} = \begin{pmatrix} \mathbf{f}_x + \mathbf{g}_x \\ \mathbf{f}_z + \mathbf{g}_z \end{pmatrix}, \tag{2.30}$$

$$\mathbf{U} = \begin{pmatrix} \mathbf{u} \\ \mathbf{v} \end{pmatrix}, \tag{2.31}$$

$$\mathbf{A} = \mathbf{M} + \mathbf{K}. \tag{2.32}$$

The entire problem can therefore be expressed as (2.33)

$$\mathbf{A}\mathbf{U}^{n+1} - \mathbf{M}\mathbf{U}^n + \mathbf{B}\mathbf{p}^{n+1} = \mathbf{b}, \tag{2.33a}$$

$$\mathbf{B^T}\mathbf{U}^{n+1} = \mathbf{0}. \tag{2.33b}$$

Penalty method is utilised for uncoupling the determination of the velocity and pressure. The mechanism that allows for this uncoupling is the relaxation of the incompressibility constraint. The pressure is found by iteration, by adding an amount λ of the divergence to the pressure value at each point. In this way, an area in which flow sinks has its pressure increased to remove the sink and enforce continuity. Similarly, an area which acts as a source has its pressure reduced.

$$\mathbf{A}\mathbf{U}^{m+1} + \mathbf{B}\mathbf{p}^{m+1} = \mathbf{b} + \mathbf{M}\mathbf{U}^n, \tag{2.34a}$$

$$\mathbf{p}^{m+1} = \mathbf{p}^m + \lambda\mathbf{B^T}\mathbf{U}^{m+1}. \tag{2.34b}$$

After calculating the value of $\mathbf{p}^{m+1}$, substitute it into (2.34b) to obtain the value of $\mathbf{U}^{m+1}$. Iteration continues until $\mathbf{p}^{m+1} = \mathbf{p}^m$. The converged value of $\mathbf{p}^{m+1}$ is the value of pressure of this time-step and will be used for calculating the pressure at the next time step through iteration again. Here, m does not refer to the time step, but the iteration step between two consecutive time steps.

$$(\mathbf{A} + \lambda\mathbf{B}\mathbf{B^T})\mathbf{U}^{m+1} = \mathbf{b} + \mathbf{M}\mathbf{U}^m - \mathbf{B}\mathbf{p}^m, \tag{2.35a}$$

$$\mathbf{p}^{m+1} = \mathbf{p}^m + \lambda\mathbf{B^T}\mathbf{U}^{m+1}. \tag{2.35b}$$

The above iteration for temporal discretisation is called Uzawa's algorithm. For Stokes flow where convective acceleration equals zero, the process of tracing backwards following the characteristics is not performed in order to remove convective acceleration.

2.3 Interfacial Boundary Condition Treatment

As reviewed before, the jump conditions at the interface are applied directly in moving mesh method. The jump of liquid properties is dealt with by using different liquid properties in different elements. The jump of stress tensor due to interfacial tension is handled through the boundary integration in (2.21).

The 2D and axisymmetric (replace x with r) formation of interfacial conditions are:

$$\left[\left(-p + 2\mu\frac{\partial u}{\partial x}\right)n_x + \mu\left(\frac{\partial u}{\partial z} + \frac{\partial v}{\partial x}\right)n_z\right]_-^+ = \sigma\kappa n_x, \qquad (2.36a)$$

$$\left[\mu\left(\frac{\partial u}{\partial z} + \frac{\partial v}{\partial x}\right)n_x + \left(-p + 2\mu\frac{\partial v}{\partial z}\right)n_z\right]_-^+ = \sigma\kappa n_z. \qquad (2.36b)$$

When assembling the matrix for a specific node, we only need to add up the integration over the triangles containing this node into the final matrices. The interfacial boundary condition is implemented naturally and neatly. In the following text, we give a proof that the static solution for a stationary bubble exists in our method, together with detailed interfacial boundary condition treatment.

Assume that there is a static solution for a circular bubble with the radius of R in 2D geometry without any external force: $\mathbf{u} = \mathbf{0}$, $p_1 - p_0 = \dfrac{\sigma}{R}$ (p_1 and p_0 are the pressure inside the bubble and outside the bubble).

Now $\mathbf{U}$ in the discretised governing equation (2.33) disappears as it equals zero and the equation turns into:

$$\mathbf{B}\mathbf{p} = \mathbf{b}. \qquad (2.37)$$

As $\mathbf{b} = (\mathbf{b}_x, \mathbf{b}_z)^T$ and $\mathbf{B} = (\mathbf{B}_x, \mathbf{B}_z)^T$, we can just consider the proof of $\mathbf{b}_x = \mathbf{B}_x\mathbf{p}$, which contains N equations (N is the total number of the nodes in the whole domain)

We consider the jth equation which is related to the jth node P. P is assumed to be a vertex node. There are K triangles which contain P and P is the j^kth node in the kth triangle (marked as Ω^k) containing it. We use ϕ_{i^k} and ψ_{i^k} to represent the P2 and P1 basis function defined at the i^kth node in Ω^k respectively and P

is the j^kth node. From (2.23) and (2.25), we obtain that in the kth triangle:

$$B_{xij}p_i = \sum_{k=0}^{K}\left(\sum_{i^k=0}^{N_{P1}}\left(\int_{\Omega^k}\frac{\partial\phi_{j^k}}{\partial x}\psi_{i^k}dxdz\right)p_{i^k}\right). \tag{2.38}$$

As each triangular element contains only one fluid, thus Ω is either inside the bubble or not. Hence p is a constant in each triangle. We let p equals p^k in Ω^k and obtain:

$$\sum_{i^k=0}^{N_{P1}}\left(\int_{\Omega^k}\frac{\partial\phi_{j^k}}{\partial x}\psi_{i^k}dxdz\right)p_{i^k} = \int_{\Omega^k}p^k\frac{\partial\phi_{j^k}}{\partial x}dxdz = \int_{\partial\Omega^k}p^k\phi_{j^k}n_x dl. \tag{2.39}$$

The jth term in the vector $\mathbf{b}_x$ is expressed as:

$$b_{xj} = \sum_{k=0}^{K}\int_{\partial\Omega^k}\left[\left(-p+2\mu\frac{\partial u}{\partial x}\right)n_x+\mu\left(\frac{\partial u}{\partial z}+\frac{\partial v}{\partial x}\right)n_z\right]\phi_{j^k}dl. \tag{2.40}$$
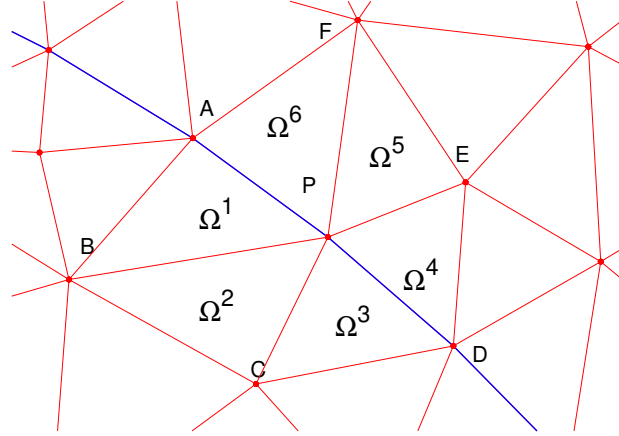

Figure 2.5: Example of a node P and all its adjacent triangles and nodes. The blue solid line represents the interface

Take the node P in Figure 2.5 as an example. Ω^1, Ω^2 and Ω^3 are inside the bubble and the pressure in these triangles is p_1. The pressure in Ω^4, Ω^5 and Ω^6 is p_0. The boundary $\partial\Omega^k$ are the three edges of the triangle Ω^k. ϕ_{j^k} equals zero along the edge which does not contain P. Hence $\int_{\partial\Omega^k}p^k\phi_{j^k}n_x dl$ and

$\int_{\partial\Omega^k} \left[\left(-p + 2\mu\frac{\partial u}{\partial x} \right) n_x + \mu \left(\frac{\partial u}{\partial z} + \frac{\partial v}{\partial x} \right) n_z \right] \phi_{j^k} dl$ equal zero on edge AB, BC, CD, DE, EF and FA.

Along the common edge of two triangles, for example BP shared by Ω^1 and Ω^2, both ϕ_{j^1} and ϕ_{j^2} equals 1 on P and 0 on B and the midpoint. Hence, they are of the same form as they are both of second order. When PB is considered as the boundary of Ω^1, the direction of the line integral is from B to P, while the direction reverses when PB is considered as the boundary of Ω^2. If the integrand is continuous, the summation of line integrals along this edge equals zero. In this example, line integrals along PB, PC, PE and PF equals zero. When the integrand is discontinuous, the summation equals the line integral of the value jump. This is how the discontinuity due to surface tension is treated and the summation is added as a source term in the right hand side vector.

Hence, in our example (2.38) and (2.40) turn into:

$$
B_{xij}p_i = \sum_{k=0}^{K} \left(\int_{\partial\Omega^k} p^k \phi_{j^k} n_x dl \right) = \int_{PA} (p_1 - p_0)\phi_j n_x dl + \int_{PD} (p_0 - p_1)\phi_j n_x dl
$$
$$
= \int_{PA} \frac{\sigma}{R}\phi_j n_x dl + \int_{DP} \frac{\sigma}{R}\phi_j n_x dl,
$$
$$
\tag{2.41}
$$

and

$$
b_{xj} = \int_{PA} \left[\left(-p + 2\mu\frac{\partial u}{\partial x} \right) n_x + \mu \left(\frac{\partial u}{\partial z} + \frac{\partial v}{\partial x} \right) n_z \right]_{-}^{+} \phi_j dl
$$
$$
+ \int_{DP} \left[\left(-p + 2\mu\frac{\partial u}{\partial x} \right) n_x + \mu \left(\frac{\partial u}{\partial z} + \frac{\partial v}{\partial x} \right) n_z \right]_{-}^{+} \phi_j dl \tag{2.42}
$$
$$
= \int_{PA} \sigma\kappa\phi_j n_x dl + \int_{DP} \sigma\kappa\phi_j n_x dl.
$$

In an ideal mesh, κ can be calculated accurately corresponding to $1/R$ and hence $b_{xj} = B_{xij}p_i$ is obtained. Similar proof can be performed at edge midpoint nodes and for $b_{zj} = B_{zij}p_i$. Hence $\mathbf{b} = \mathbf{Bp}$ holds and there exists a static solution for circular bubble at numerical level in our method.

2.4   Method of Characteristic

In our method, method of characteristic is used to deal with the material derivative $\dfrac{d\mathbf{u}}{dt}$. The characteristic foot and the triangle in which the foot is are identified. The value of $\mathbf{u}$ on the characteristic foot at last time step is obtained by interpolation of all nodes in this triangle. In our method, the velocity is a linear combination of the basis functions defined on the vertices and edge midpoints. It is worthwhile to mention that the interpolation for vertices and edge midpoints are actually different. For simplicity, P2 method of characteristic in 1D situation for the linear convection equation:

$$\frac{\partial u}{\partial t} + a\frac{\partial u}{\partial x} = 0, \ a > 0, \tag{2.43}$$
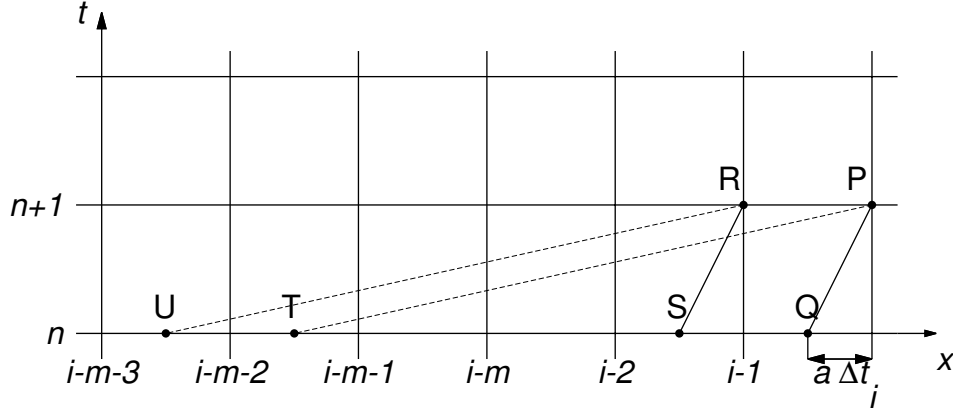
is considered.

Figure 2.6: P2 method of characteristic in 1D situation: the approximated solution is a quadratic function in one element (x_i, x_{i-1} and x_{i-2} are in the same element); Δt is the temporal step and $\Delta x = x_i - x_{i-1}$ is the spatial step

The exact solution is constant along the characteristic line (PQ and RS in Figure 2.6) and therefore $u_i^{n+1} = u(P) = u(Q)$ and $u_{i-1}^{n+1} = u(R) = u(S)$ are attained. The value on S and Q are obtained by interpolation in the element which contains 3 nodes: x_i, x_{i-1} and x_{i-2}:

$$u_i^{n+1} = f_1(u_{i-2}^n, u_{i-1}^n, u_i^n)$$
$$= u_{i-2}^n \frac{a\Delta t(a\Delta t - \Delta x)}{2(\Delta x)^2} + u_{i-1}^n \frac{a\Delta t(2\Delta x - a\Delta t)}{(\Delta x)^2} + u_i^n \frac{(\Delta x - a\Delta t)(2\Delta x - a\Delta t)}{2(\Delta x)^2},$$
$$(2.44)$$

$$u_{i-1}^{n+1} = f_2(u_{i-2}^n, u_{i-1}^n, u_i^n)$$
$$= u_{i-2}^n \frac{a\Delta t(a\Delta t + \Delta x)}{2(\Delta x)^2} + u_{i-1}^n \frac{(a\Delta t + \Delta x)(\Delta x - a\Delta t)}{(\Delta x)^2} + u_i^n \frac{a\Delta t(a\Delta t - \Delta x)}{2(\Delta x)^2}.$$
$$(2.45)$$

When the characteristic foot of a node falls into the element which contains this node (small Courant−Friedrichs−Lewy (CFL) number), (2.44) is equivalent to Beam-Warming scheme and (2.45) is equivalent to central difference scheme. However, method of characteristic allows the foot of a node to fall into an element which does not contain the node. For example, if PT and RU in Figure 2.6 are the characteristic lines, the element containing the foot has to be identified before interpolation. Take P's characteristic foot T for example.

If the element contains x_{i-m-3}, x_{i-m-2} and x_{i-m}, the interpolation takes the form of (2.44):
$$u_i^{n+1} = f_1(u_{i-m-3}, u_{i-m-2}, u_{i-m-1}). \qquad (2.46)$$

If the element contains x_{i-m-2}, x_{i-m-1} and x_{i-m}, the interpolation takes the form of (2.45):
$$u_i^{n+1} = f_2(u_{i-m-2}, u_{i-m-1}, u_{i-m}). \qquad (2.47)$$

When CFL number is small, P2 method of characteristic can be described as a hybrid of Beam-Warming scheme and central difference scheme. When CFL number is sufficiently large and the foot is no longer in the same element with the node, the interpolation (extrapolation will not take place) is ensured but the form is not certain. Although a theoretical analysis on the stability of P2 method of characteristic has not been given, our numerical practise has showed that this method is stable.

2.5 Mesh Generator

For the success of the moving mesh method, it is crucial to maintain a valid and high quality mesh. The adaptive mesh generator developed by Li (2013) is employed in the study for generating the initial mesh and for constantly remeshing in computation. Two strategies are possible for remeshing method: local-arrangement of the mesh at each time step and occasional complete remeshing. The first one is adopted in the mesh generator.
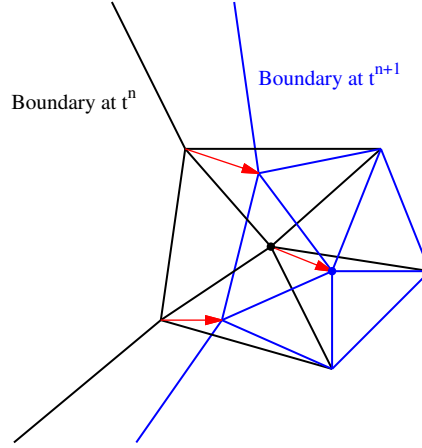

Figure 2.7: Example of mesh movement near the moving boundary: $\rightarrow$ represents the movement of the boundary nodes or relocation of the interior vertex

Three algorithms are utilised to adapt the mesh:

1. The motion of the vertices on the moving boundary (interface) is determined by its velocity. As the interface evolves, the new positions of the vertices on the interface are computed by a Lagrangian method. The interior nodes near the moving boundary are also relocated to keep them away from the moving boundary. The mesh movement is illustrated in 2.7.

2. Edges not on the interface are swapped according to the Delaunay condition. A circumcircle is drawn using the vertices of each triangle. If a node from another triangle lies within this circle, the common edge for the two triangles
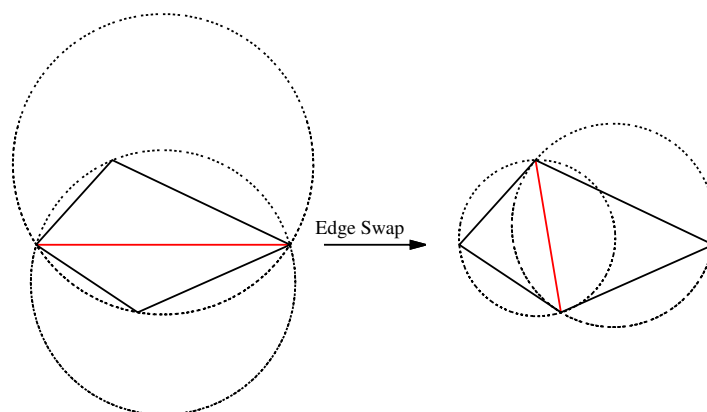
Figure 2.8: Example of edge swap operation to satisfy Delaunay condition

swaps to another position in order to keep that the circumcircle of each triangle does not contain any vertices from other triangles. Edge swapping is showed in Figure 2.8.
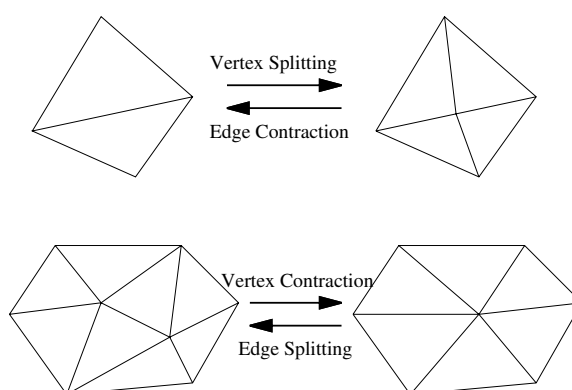

Figure 2.9: Examples of Edge/Vertex splitting/contraction

3. Edge splitting/contraction are performed to refine/coarsen the mesh (Figure 2.9). Edge splitting divide one edge into two segments and generate a new vertex. The vertex splitting divide one vertex into two. the reverse operations are vertex contraction and edge contraction respectively.

Chapter 3

Method Development

One main part of the study is the flow solver for multiphase flows with temperature effect. Hence heat transfer equation is taken into consideration, as well as temperature dependence of fluid properties and dissipation due to viscosity.

The overall governing equations in vector form are:

$$\rho \frac{d\mathbf{u}}{dt} = -\nabla p + \nabla \cdot \left[\mu \left((\nabla \mathbf{u}) + (\nabla \mathbf{u})^{\mathbf{T}} \right) \right] + \rho \mathbf{g}, \tag{3.1a}$$

$$\rho c_v \frac{dT}{dt} = -\nabla(k\nabla T) + \Phi, \tag{3.1b}$$

$$\nabla \cdot \mathbf{u} = 0, \tag{3.1c}$$

$$\rho = \rho_0 - \alpha(T - T_0), \tag{3.1d}$$

$$\sigma = \sigma_0 - \beta(T - T_0), \tag{3.1e}$$

$$Interface\ B.C. : [(-p\mathbf{I} + \mu\mathbf{D}) \cdot \mathbf{n}]_-^+ = \sigma\kappa\mathbf{n} - \nabla\sigma, \tag{3.1f}$$

where $\mathbf{D}$ represents the strain rate tensor, Φ represents the dissipation function and T_0 is the reference temperature. They are defined as:

$$\mathbf{D} = \frac{1}{2} \left[(\nabla \mathbf{u}) + (\nabla \mathbf{u})^{\mathbf{T}} \right], \tag{3.2a}$$

$$\Phi = 2\mu D_{ij} D_{ij}. \tag{3.2b}$$

In two dimension situation, dissipation function is expressed as:

$$\Phi_{xz} = \mu \left[2 \left(\frac{\partial u}{\partial x} \right)^2 + 2 \left(\frac{\partial v}{\partial z} \right)^2 + \left(\frac{\partial u}{\partial z} + \frac{\partial v}{\partial x} \right)^2 \right]. \tag{3.3}$$

In axisymmetric situation, dissipation function is expressed as:

$$\Phi_{rz} = \mu \left[2\left(\frac{\partial u}{\partial r}\right)^2 + 2\left(\frac{u}{r}\right)^2 + 2\left(\frac{\partial v}{\partial z}\right)^2 + \left(\frac{\partial u}{\partial z} + \frac{\partial v}{\partial r}\right)^2 \right]. \tag{3.4}$$

Our aim is to develop a flow solver for the above equations based on a moving mesh. Dissipation, heat transfer and temperature dependence of fluid properties are to be considered. In order to improve the accuracy in interface representation and reduce spurious current, the isoparametric finite element method are to be developed. We have already developed isoparametric method for the flow solver on fixed mesh and added dissipation, heat transfer and density variation in the code. This chapter presents the development to date.

3.1 Coupling Heat Transfer Equation

3.1.1 Weak Formulation

The heat transfer equations in two-dimensional and axisymmetric cases are as followed:

$$\rho c_v \frac{dT}{dt} = -\frac{\partial}{\partial x}\left(k\frac{\partial T}{\partial x}\right) - \frac{\partial}{\partial z}\left(k\frac{\partial T}{\partial z}\right) + \Phi_{xz}, \tag{3.5}$$

and

$$\rho c_v \frac{dT}{dt} = -\frac{1}{r}\frac{\partial}{\partial r}\left(r\frac{\partial T}{\partial r}\right) - \frac{\partial}{\partial z}\left(k\frac{\partial T}{\partial z}\right) + \Phi_{rz}. \tag{3.6}$$

In the following text, we only discuss the weak formulation and discretisation for heat transfer equation in 2D situation. The weak formulation in 2D is:

$$\int_\Omega \rho c_v \phi \frac{dT}{dt} dxdz - \int_\Omega k\frac{\partial T}{\partial x}\frac{\partial \phi}{\partial x} dxdz - \int_\Omega k\frac{\partial T}{\partial z}\frac{\partial \phi}{\partial z} dxdz$$
$$= -\int_{\partial\Omega}\left(k\frac{\partial T}{\partial x}n_x + k\frac{\partial T}{\partial z}n_z\right)\phi dl + \int_\Omega \Phi_{xz}\phi dxdz. \tag{3.7}$$

3.1.2 Discretisation

The temperature field is approximated on the triangulation using P2 element and thus temperature is quadratic in each element and continuous over the entire

region. Hence the weak formulation turns into:

$$\sum_{j=0}^{5} \left(\int_{\Omega} \rho c_v \phi_i \phi_j dx dz \right) \frac{dT_j}{dt} - \sum_{j=0}^{5} \left(\int_{\Omega} k \left(\frac{\partial \phi_i}{\partial x} \frac{\partial \phi_j}{\partial x} + \frac{\partial \phi_i}{\partial z} \frac{\partial \phi_j}{\partial z} dx dz \right) \right) T_j \quad (3.8a)$$

$$= - \int_{\partial \Omega} g_T \phi_i dl + \Phi_{xz},$$

$$\Phi_{xz} = \sum_{j=0}^{5} \sum_{k=0}^{5} \left[\left(\int_{\Omega} \mu \left(2 \frac{\partial \phi_j}{\partial x} \frac{\partial \phi_k}{\partial x} + \frac{\partial \phi_j}{\partial z} \frac{\partial \phi_k}{\partial z} \right) \phi_i dx dz \right) u_j u_k \quad (3.8b)$$

$$+ \left(\int_{\Omega} 2\mu \frac{\partial \phi_j}{\partial z} \frac{\partial \phi_k}{\partial x} \phi_i dx dz \right) u_j v_k + \left(\int_{\Omega} \mu \left(\frac{\partial \phi_j}{\partial x} \frac{\partial \phi_k}{\partial x} + 2 \frac{\partial \phi_j}{\partial z} \frac{\partial \phi_k}{\partial z} \right) \phi_i dx dz \right) v_j v_k \right].$$

The discretised equations can be written as matrices:

$$\mathbf{M}_T \frac{d\mathbf{T}}{dt} + \mathbf{K}_T \mathbf{T} = \mathbf{g} + \mathbf{\Phi}. \quad (3.9)$$

3.1.3   Solution

The material derivative of the temperature is discretised as followed:

$$\frac{d\mathbf{T}}{dt} \approx \frac{\mathbf{T}^{n+1} - \mathbf{T}^n}{\Delta t}. \quad (3.10)$$

Hence, the heat transfer equation is written as:

$$\mathbf{A}_T \mathbf{T}^{n+1} - \frac{\mathbf{M}_T}{\Delta t} \mathbf{T}^n = \mathbf{g} + \mathbf{\Phi}, \quad (3.11)$$

in which $\mathbf{A}_T = \mathbf{M}_T / \Delta t + \mathbf{K}_T$.

The coupling of heat transfer equation and Navier-Stokes equations include varied density, varied surface tension (this part of work has not been carried out), heat convection and dissipation. The density variation is modeled with Boussinesq approximation, by adding a buoyancy source term $\Delta \rho g$ in the Navier-Stokes equation. Heat convection is solved by finding the temperature of the previous time step following the characteristics backwards. The dissipation term is highly non-linear and hence we adopt the strategy that first solves Navier-Stokes equation and then uses the determined velocity to calculate the dissipation term.

The solution steps are: 1. Solve Navier Stokes equation (2.33) and use the temperature of previous time step to determine buoyancy source term:

$$\mathbf{A}\mathbf{U}^{n+1} - \mathbf{M}\mathbf{U}^n + \mathbf{B}\mathbf{p}^{n+1} = \mathbf{b}^{n+1} + \mathbf{G}(\mathbf{T}^n), \tag{3.12a}$$

$$\mathbf{B^T}\mathbf{U}^{n+1} = \mathbf{0}, \tag{3.12b}$$

$$\tag{3.12c}$$

2. Solve heat transfer equation and add dissipation using the velocity just determined:

$$\mathbf{A}_T\mathbf{T}^{n+1} - \frac{\mathbf{M}_T}{\Delta t}\mathbf{T}^n = \mathbf{g}^{n+1} + \mathbf{\Phi}(\mathbf{u}^{n+1}). \tag{3.13}$$

3.2 Isoparametric Finite Element Method Development

The advantage of using a curved element method is to obtain a better representation of the curved boundary. In our study, a better representation of the interface can help to reduce spurious currents. P2 finite element method use 6 nodes on the three vertices and three edge midpoints. When the boundary is approximated through piecewise straight line segment in P2 element method, the edge midpoints are actually not on the interface. Refining the mesh can reduce the deviation of edge midpoints from the interface. However, if a technique is utilised to put the edge midpoints on the interface, boundary conditions can be imposed on the real boundary nodes correctly and the boundary can be fitted by piecewise curved line segment.

For simplicity, we only let the edge on the curved boundary be curved. Firstly, the edge midpoints are to be put on the interface. Considering that in most cases, the curved boundary we are dealing with are circular boundary, the edge midpoint is moved to the midpoint of the arc between the two vertices. This is illustrated in Figure 3.1.

With six known coordinates, the next step is to find the mapping from the referenced triangle to this curved triangle. Using the basis functions defined as $\varphi_i(s_j, t_j) = \delta_{ij}$
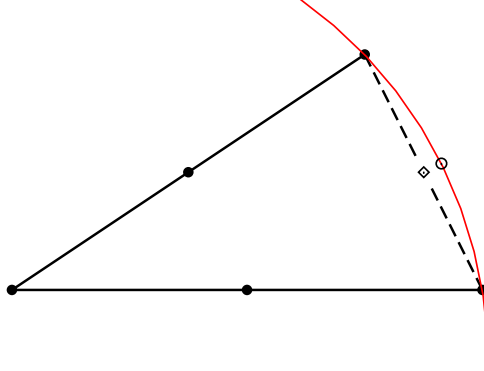
Figure 3.1: Example of moving an edge midpoint to the circular edge: ∘ represents the position after moving and ⋄ represents previous position

$$x = \sum_{i=0}^{5} x_i \varphi_i(s,t), \ \ y = \sum_{i=0}^{5} y_i \varphi_i(s,t). \tag{3.14}$$

Since we only consider one curved edge, only one edge midpoint (node 3 in Figure 3.2) is moved to the curve and the transformation is:

$$\begin{pmatrix} x \\ y \end{pmatrix} = \begin{pmatrix} x_0 \\ y_0 \end{pmatrix} + \begin{pmatrix} x_1 - x_0 & x_2 - x_0 \\ y_1 - y_0 & y_2 - y_0 \end{pmatrix} \begin{pmatrix} s \\ t \end{pmatrix} + \begin{pmatrix} 4x_3 - 2x_1 - 2x_2 \\ 4y_3 - 2y_1 - 2y_2 \end{pmatrix} st. \tag{3.15}$$

Different from P2 finite element method, this isoparametric mapping results in a non-linear Jacobian matrix:

$$\mathbf{J} = \frac{\partial(x,y)}{\partial(s,t)} = \begin{pmatrix} x_1 - x_0 + (4x_3 - 2x_1 - 2x_2)t & x_2 - x_1 + (4x_3 - 2x_1 - 2x_2)s \\ y_1 - y_0 + (4y_3 - 2y_1 - 2y_2)t & y_2 - y_0 + (4y_3 - 2y_1 - 2y_2)s \end{pmatrix}. \tag{3.16}$$

Similarly, the integrals over a curved triangles are approached through (2.16).

It is worth to mention that this Jacobian matrix transforms the straight linear segment $s + t = 1$ in $s - t$ plane into a second order curved segment in $x - y$ plane:

$$\begin{cases} x = x_2 + (-x_1 - 3x_2 + 4x_3)s + (2x_1 + 2x_2 - 4x_3)s^2 \\ y = y_2 + (-y_1 - 3y_2 + 4y_3)s + (2y_1 + 2y_2 - 4y_3)s^2 \end{cases}, \tag{3.17}$$

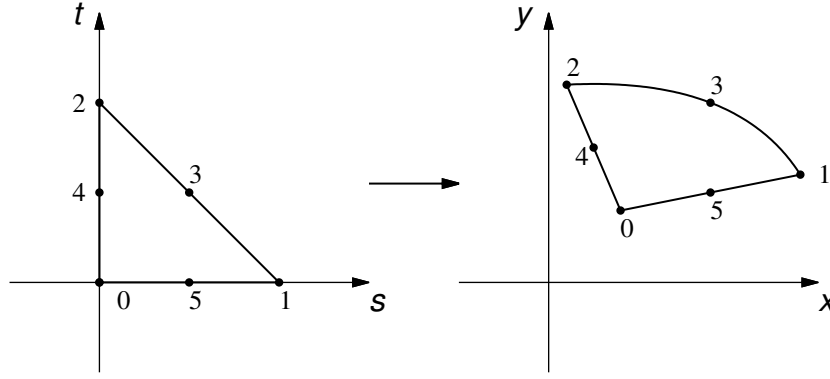in which the range of s is $[0, 1]$.

Figure 3.2: Example of the transformation from a referenced triangle in $s - t$ plane to a curved edge triangle in $x - y$ plane

In the Navier-Stokes solver the velocity of previous time step, which is the velocity on characteristic foot, is achieved by interpolation of the velocity at the six nodes in the triangles. It is different in a curved triangle as the mapping is non-linear and it is crucial to find the value of six basis functions on the characteristic foot. This is achieved by obtain (s, t) in the referenced triangle given a curved triangle and (x, y) in the curved triangle. Newton-Raphson iterative method is employed. The algorithm of the iteration is as followed:

1. Find an initial solution (assuming the curved edge is straight).

$$s_0 = \frac{(y - y_0)(x_2 - x_0) - (y_2 - y_0)(x - x_0)}{(y_1 - y_0)(x_2 - x_0) - (y_2 - y_0)(x_1 - x_0)}, \tag{3.18a}$$

$$t_0 = \frac{(y - y_0)(x_1 - x_0) - (y_1 - y_0)(x - x_0)}{(y_1 - y_0)(x_2 - x_0) - (y_2 - y_0)(x_1 - x_0)}. \tag{3.18b}$$

2. Calculate the corresponding point $(\tilde{x}, \tilde{y})$ of (s_n, t_n) (n is used to mark the iteration time) in the curved triangle and examine the the deviation of $(\tilde{x}, \tilde{y})$ from

the given (x, y):

$$\tilde{x} = x_0 + (x_1 - x_0)s_n + (x_2 - x_0)t_n + (4x_3 - 2x_1 - 2x_2)s_n t_n, \qquad (3.19\text{a})$$

$$\tilde{y} = y_0 + (y_1 - y_0)s_n + (y_2 - y_0)t_n + (4y_3 - 2y_1 - 2y_2)s_n t_n, \qquad (3.19\text{b})$$

$$a_n = \tilde{x} - x, \qquad (3.19\text{c})$$

$$b_n = \tilde{y} - y. \qquad (3.19\text{d})$$

If the deviation is small enough, (s_n, t_n) is the solution. Otherwise, continue the iteration.

3. Assume that (s_{n+1}, t_{n+1}) is the solution and the deviation (a_{n+1}, b_{n+1}) equals zero. Expand (a_{n+1}, b_{n+1}) into Taylor series and let them equal zero:

$$a_{n+1} = a_n + \frac{\partial a}{\partial s}(s_n, t_n)(s_{n+1} - s_n) + \frac{\partial a}{\partial t}(s_n, t_n)(t_{n+1} - t_n) = 0, \qquad (3.20\text{a})$$

$$b_{n+1} = b_n + \frac{\partial b}{\partial s}(s_n, t_n)(s_{n+1} - s_n) + \frac{\partial b}{\partial t}(s_n, t_n)(t_{n+1} - t_n) = 0. \qquad (3.20\text{b})$$

By solving the linear equations, (s_{n+1}, t_{n+1}) is attained and go to step 2 to examine the deviation. Note that:

$$\begin{pmatrix} \dfrac{\partial a}{\partial s} & \dfrac{\partial a}{\partial t} \\[2mm] \dfrac{\partial b}{\partial s} & \dfrac{\partial b}{\partial t} \end{pmatrix} = \begin{pmatrix} \dfrac{\partial x}{\partial s} & \dfrac{\partial x}{\partial t} \\[2mm] \dfrac{\partial y}{\partial s} & \dfrac{\partial y}{\partial t} \end{pmatrix}. \qquad (3.21)$$

When (s, t) is obtained, the velocity on characteristic foot can be calculated by interpolation:

$$u = \sum_{i=0}^{5} u_i \phi_i(x, y) = \sum_{i=0}^{5} u_i \varphi_i(s, t), \qquad (3.22\text{a})$$

$$v = \sum_{i=0}^{5} v_i \phi_i(x, y) = \sum_{i=0}^{5} v_i \varphi_i(s, t). \qquad (3.22\text{b})$$

Chapter 4

Validation

4.1 Poisson Solver

Before presenting the validation results for the Navier-Stokes equations, it is worthwhile to discuss the performance of P2 and isoparametric P2 finite element method on boundary value problems in 2D and axisymmetric geometries.

A ring mesh is considered and an example of the mesh in $x - z$ plane is illustrated in Figure 4.1a. The close-up of the circular boundary in Figure 4.1b shows that in isoparametric P2 elements, nodes on boundary edge are put on the circular boundary and the boundary is represented by piecewise second-order curved segments. We can see from the close-up that the piecewise second-order curved segment fits the real circular boundary far better that piecewise line segment in P2 method.

Consider a Poisson equation in 2D ring domain ($x = r cos\theta, \ z = r sin\theta$):

$$\Delta_2 u = \frac{1}{r^2} \frac{\partial}{\partial r} \left(r \frac{\partial u}{\partial r} \right) + \frac{1}{r^2} \frac{\partial^2 u}{\partial \theta^2} = 1, \ 1 < r < 2, \tag{4.1a}$$

$$u|_{r=1} = cos^2\theta, \tag{4.1b}$$

$$u|_{r=2} = sin^2\theta. \tag{4.1c}$$

The analytical solution is:

(a) Ring mesh

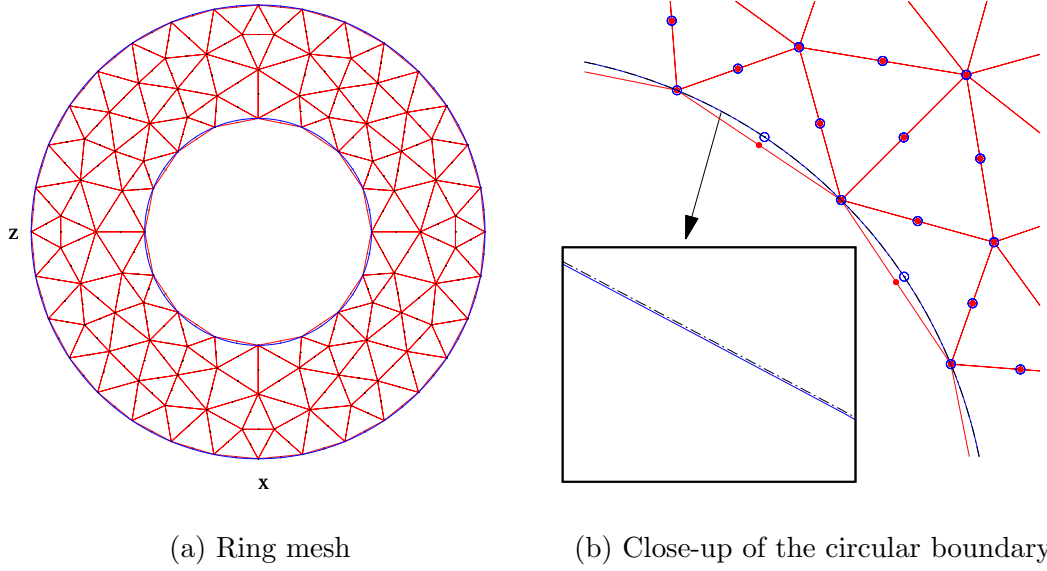(b) Close-up of the circular boundary

Figure 4.1: Example of a ring mesh used in calculation: (a) red lines represent the P2 finite element mesh and blue curves are piecewise second order curved; (b) black dashed line represents the circular boundary and red and blue circular dots are nodes in P2 and curved P2 elements respectively

$$u(r,\theta) = -\frac{1}{2} + \frac{r^2}{4} + \frac{3}{4}\Big(1 - \frac{lnr}{ln2}\Big) - \frac{1}{6}\Big(r^2 - \frac{4}{r^2}\Big)cos2\theta. \tag{4.2}$$

The error is calculated as the average error over the domain:

$$E_h = \frac{\int_\Omega |u_h - u| dxdz}{\int_\Omega dxdz}. \tag{4.3}$$

Consider a Poisson equation in a spherical coordinate:

$$\Delta_3 u = \frac{1}{r^2}\frac{\partial}{\partial r}\Big(r^2\frac{\partial u}{\partial r}\Big) + \frac{1}{r^2 sin\theta}\frac{\partial}{\partial \theta}\Big(sin\theta\frac{\partial u}{\partial \theta}\Big) + \frac{1}{r^2 sin^2\theta}\frac{\partial^2}{\partial \phi^2} = 6, \ 1 < r < 2, \tag{4.4a}$$

$$u|_{r=1} = 1, \tag{4.4b}$$

$$u|_{r=2} = 4. \tag{4.4c}$$

The analytical solution is:

$$u = r^2. \tag{4.5}$$

As the boundary condition has nothing to do with ϕ, it can be solved using the axisymmetric Poisson solver ($x = r\cos\theta$, $z = r\sin\theta$). Similarly, the error is calculated as the average error over the domain:

$$E_h = \frac{\int_\Omega |u_h - u| x\,dx\,dz}{\int_\Omega x\,dx\,dz}. \tag{4.6}$$

P2 and isoparametric P2 finite element methods are applied to solve (4.1) and (4.4) with four increasingly finer triangulations. The error from different triangulations using P2 and isoparametric P2 approximation are shown in Table 4.1 and plotted in Figure 4.2. Note that N_{T_h} represents the number of triangles in the mesh and E_h^{P2} and E_h^{P2i} represent the numerical error in P2 method and in isoparametric P2 method respectively.

	2D solver		Axisymmetric solver	
N_{T_h}	E_h^{P2}	E_h^{P2i}	E_h^{P2}	E_h^{P2i}
348	0.0685265	0.0062813	0.157933	0.0429844
656	0.0222541	0.00192525	0.0896128	0.0033376
1346	0.00551967	0.000647393	0.0224366	0.00108501
2528	0.00562069	0.000496435	0.0224476	0.000929374

Table 4.1: Error of P2 and isoparametric P2 approximation for 2D and axisymmetric Poisson solvers.

Second order convergence is obtained for both methods as the number of triangles increases, which is shown in Figure 4.2. The error from isoparametric P2 method is always smaller than that from P2 method and the error from isoparametric P2 method is around one tenth of that from P2 method. The reduction in error is contributed by the better representation of the boundary. From Figure 4.1, in P2 method, the boundary condition is applied on piecewise linear segments, while in isoparametric P2 method, the boundary condition is applied on piecewise second-order curved segments.
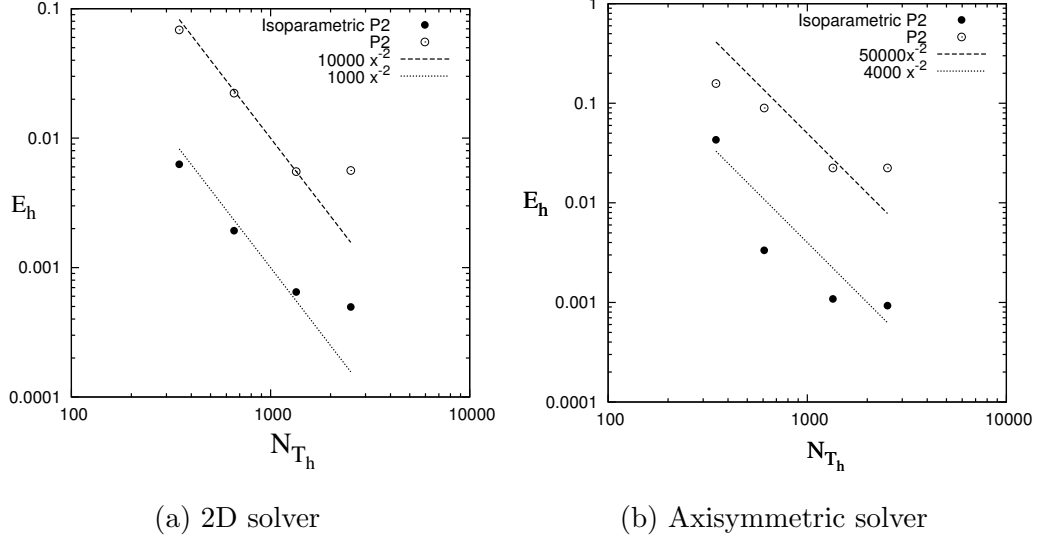
(a) 2D solver

(b) Axisymmetric solver

Figure 4.2: Numerical errors are reduced with an order of two with the increase in the number of triangles

4.2 Flow Solver

In order to validate the isoparametric finite element flow solver, we choose two benchmark problems with circular boundaries: Stokes flow past a sphere and lid-driven flow in a polar cavity.

4.2.1 Stokes Flow Past A Sphere

A Stokes flow past a sphere with a radius a is illustrated in Figure 4.3 and the uniform velocity at the far field is U. The analytical solution $\mathbf{u} = (u_r, u_\theta)$ is:

$$u_r = U cos\theta \left(1 + \frac{a^3}{2r^3} - \frac{3a}{2r} \right), \tag{4.7a}$$

$$u_\theta = -U sin\theta \left(1 - \frac{a^3}{4r^3} - \frac{3a}{4r} \right). \tag{4.7b}$$

This problem is solved numerically by the axisymmetric solver on a rectangular domain (Figure 4.4). The left edge is the axisymmetric axis. The numerical
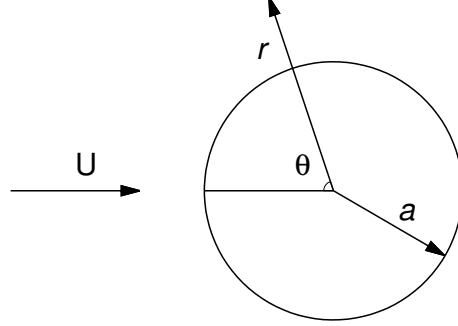
47

Figure 4.3: Stokes flow past a sphere

code can only deal with a finite computing domain, while in this problem, far field conditions are given. Hence, the analytical solution is imposed on the other edges and the no-slip boundary is imposed on the circular boundary.

N_{T_h}	E_h^{P2}	E_h^{P2i}
51	1.1813×10^{-5}	5.1662×10^{-6}
358	5.0086×10^{-6}	2.4165×10^{-7}
1007	4.4997×10^{-8}	1.7566×10^{-8}
11686	1.5830×10^{-8}	1.6280×10^{-9}

Table 4.2: Numerical error for calculating Stokes flow past a sphere

The numerical error of velocity for both methods using different triangulations are presented in Table 4.2 using an average of the whole domain:

$$E_h = \frac{\int_\Omega \sqrt{(u_h - u)^2 + (v_h - v)^2}\, r\, dr\, dz}{\int_\Omega r\, dr\, dz} \tag{4.8}$$

The isoparametric element method always performed better than straight element method. The results validate the flow solver with isoparametric element on Stokes flow and its better performance.
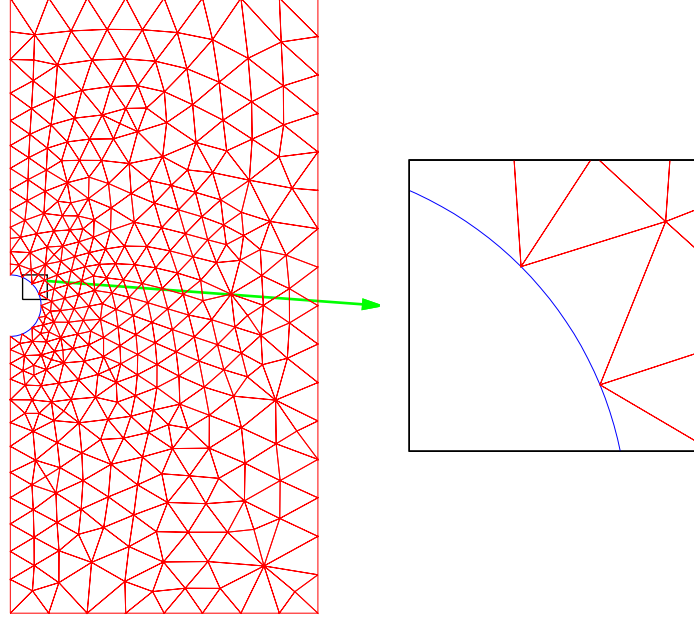
Figure 4.4: The computing domain and the close-up near the circular boundary (blue line for the second-order curved edge and red line for straight edge)

4.2.2 Lid-driven Flow in A Polar Cavity

The lid-driven flow in a two-dimensional polar cavity is examined with isoparametric finite element Navier-Stokes solver. The geometry is as illustrated in Figure 4.5a and no-slip velocity condition is imposed on the outer circular boundary and both side walls. The radial and azimuthal velocity on the inner circular boundary equal 0 and U_0 respectively. This flow is characterised by $Re = \rho U_0 L / \mu$ number and L corresponds the difference between the radius of the inner and outer circular boundaries.

The radial and azimuthal velocity profiles along the radial line $\theta = 0$ are plotted and both numerical experimental results of Fuchs and Tillmark (1985) are included for comparison (Figure 4.5b). Good agreement with previous numerical results has been achieved. The discrepancy between the numerical and experimental data may be the result of the three-dimensional effects in the experiment.
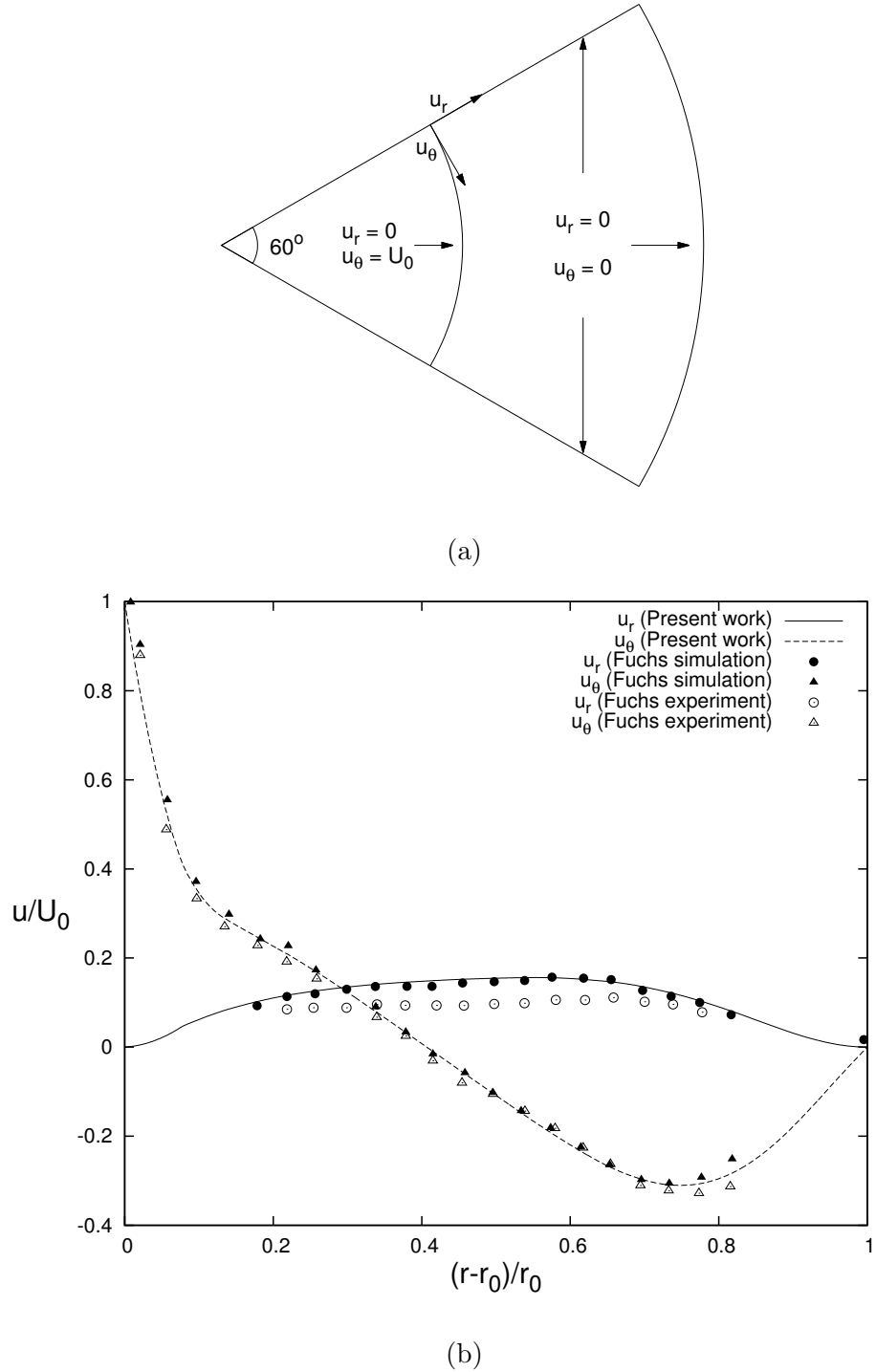
(a)

(b)

Figure 4.5: (a) Geometry of lid-driven flow in a polar cavity; (b) Comparison of the radial u_r and azimuthal u_θ velocity profiles along the radial line $\theta = 0$ (Re = 350)

50

4.3 Convection Solver

4.3.1 Natural Convection in A Square Cavity

The numerical experiment of natural convection in a square cavity is conducted to test the validity of the convection solver. The geometry of the square cavity is illustrated in Figure 4.6.
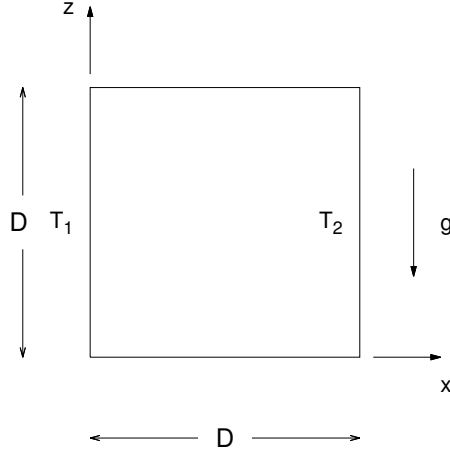

Figure 4.6: Two-dimensional flow in a square cavity of side D

A two-dimensional flow of a Boussinesq fluid of $Pr = \nu/\kappa = 0.71123$ is considered and $Ra = \beta g(T_1 - T_2)D^3/\kappa\nu$ is used to characterised the flow. Both velocity components are zero on the boundaries. The horizontal walls are insulated and the vertical sides are at temperature T_1 and T_2 respectively. The solution of this problem—velocities, temperature and rates of heat transfer—have been obtained for $Ra = 10^3$, 10^4, 10^5 and 10^6. Contour maps for temperature is drawn in Figure 4.7. Note that the results are presented in non-dimensional form: $\tilde{T} = (T - T_2)/(T_1 - T_2)$, $\tilde{u} = uD/\kappa$, $\tilde{w} = uD/\kappa$, $\tilde{x} = x/D$ and $\tilde{z} = z/D$.

The following is examined and compared with benchmark results (detailed explanation of Nusselt number can be seen in (de Vahl Davis, 1983)):
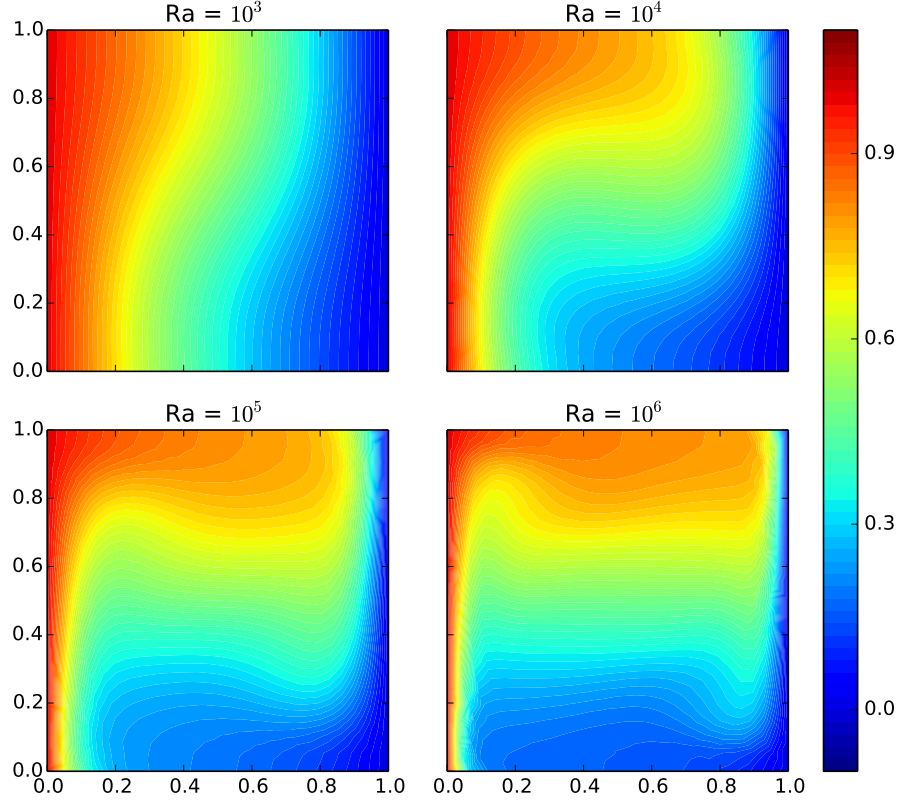
Figure 4.7: Contour maps of non dimensional temperature $\tilde{T}$ for $Ra = 10^3$, 10^4, 10^5, 10^6.

1. maximum and minimum vertical velocity ($\tilde{w}_{max}$ and $\tilde{w}_{min}$) on the horizontal mid-plane ($\tilde{x} = 0.5$) and its location;

2. maximum and minimum horizontal velocity ($\tilde{u}_{max}$ and $\tilde{u}_{min}$) on the vertical mid-plane ($\tilde{z} = 0.5$) and its location;

3. average Nusselt number, $\overline{Nu} = \int_{\Omega}(\tilde{u}\tilde{T} - \frac{\partial \tilde{T}}{\partial \tilde{x}})d\Omega$;

4. average Nusselt number on the horizontal mid-plane $Nu_{\frac{1}{2}}$ and the left wall boundary Nu_0;

5. maximum and minimum local Nusselt number Nu_{max} and Nu_{min} on the hot wall.

	Ra							
	Benchmark solution				Present work			
	10^3	10^4	10^5	10^6	10^3	10^4	10^5	10^6
$\tilde{u}_{max}$	3.649	16.178	34.730	64.630	3.6488	16.215	34.756	66.641
$\tilde{z}_{\tilde{u}_{max}}$	0.813	0.823	0.855	0.850	0.813	0.824	0.856	0.849
$\tilde{w}_{max}$	3.697	19.617	68.590	219.36	3.698	19.670	68.591	225.19
$\tilde{x}_{\tilde{w}_{max}}$	0.178	0.119	0.066	0.0379	0.178	0.120	0.065	0.0380
$\overline{Nu}$	1.118	2.243	4.519	8.800	1.118	2.244	4.525	8.928
$Nu_{\frac{1}{2}}$	1.118	2.243	4.519	8.799	1.112	2.245	4.526	8.934
Nu_0	1.117	2.238	4.509	8.817	1.126	2.282	4.527	8.510
Nu_{max}	1.505	3.528	7.717	17.925	1.507	3.553	7.763	18.707
Nu_{min}	0.692	0.586	0.729	0.989	0.691	0.587	0.716	1.008

Table 4.3: Comparison with benchmark solution in de Vahl Davis and Jones (1983)

From the comparison results in Table 4.3, good quantitative agreement has been obtained for most examined items with relative error less than 5%.

4.3.2 Natural Convection in An Annulus

The natural convection in cylindrical horizontal annulus is studied. The geometry is illustrated as Figure 4.8a. The flow is characterised by $Ra = \beta g(T_i - T_o)(R_o - R_i)^3/\kappa\nu$, $Pr = \nu/\kappa$ and $\eta = R_o/R_i$.

In our simulation, $\eta = 2.6$ and $Pr = 0.71$. The solution has been obtained for $Ra = 10^2$, 10^3, 10^4 and 10^5 (Figure 4.8b, note that the length of the arrow does not represent the magnitude of the velocity). The temperature distribution and velocity profile are plotted and are compared with the simulation results of Padilla et al. (2006). Good agreement has been obtained.
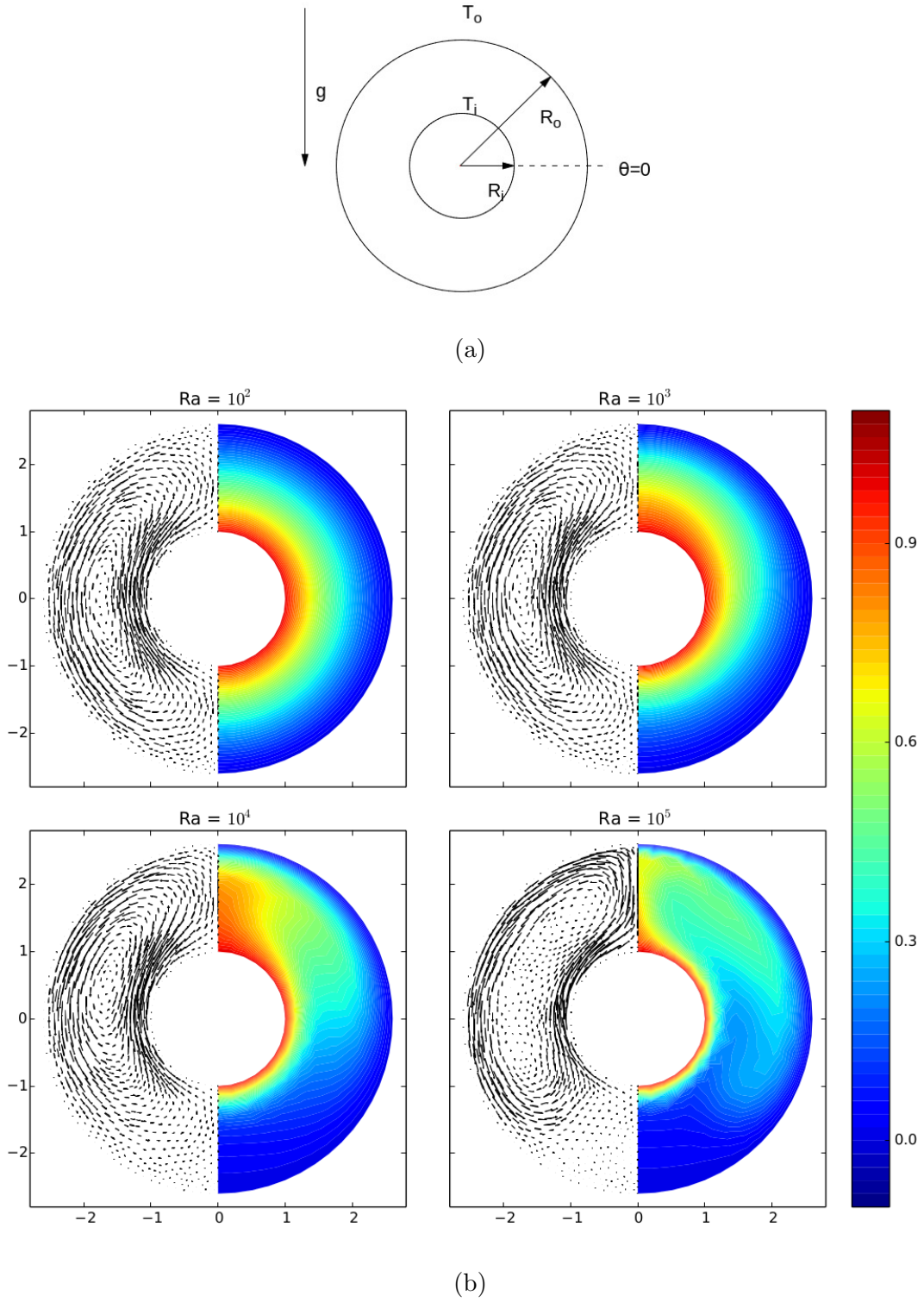
(a)

(b)

Figure 4.8: (a) The geometry of the annulus between two coaxial cylinders; (b) Velocity field and temperature distribution for $Ra = 10^2$, 10^3, 10^4 and 10^5
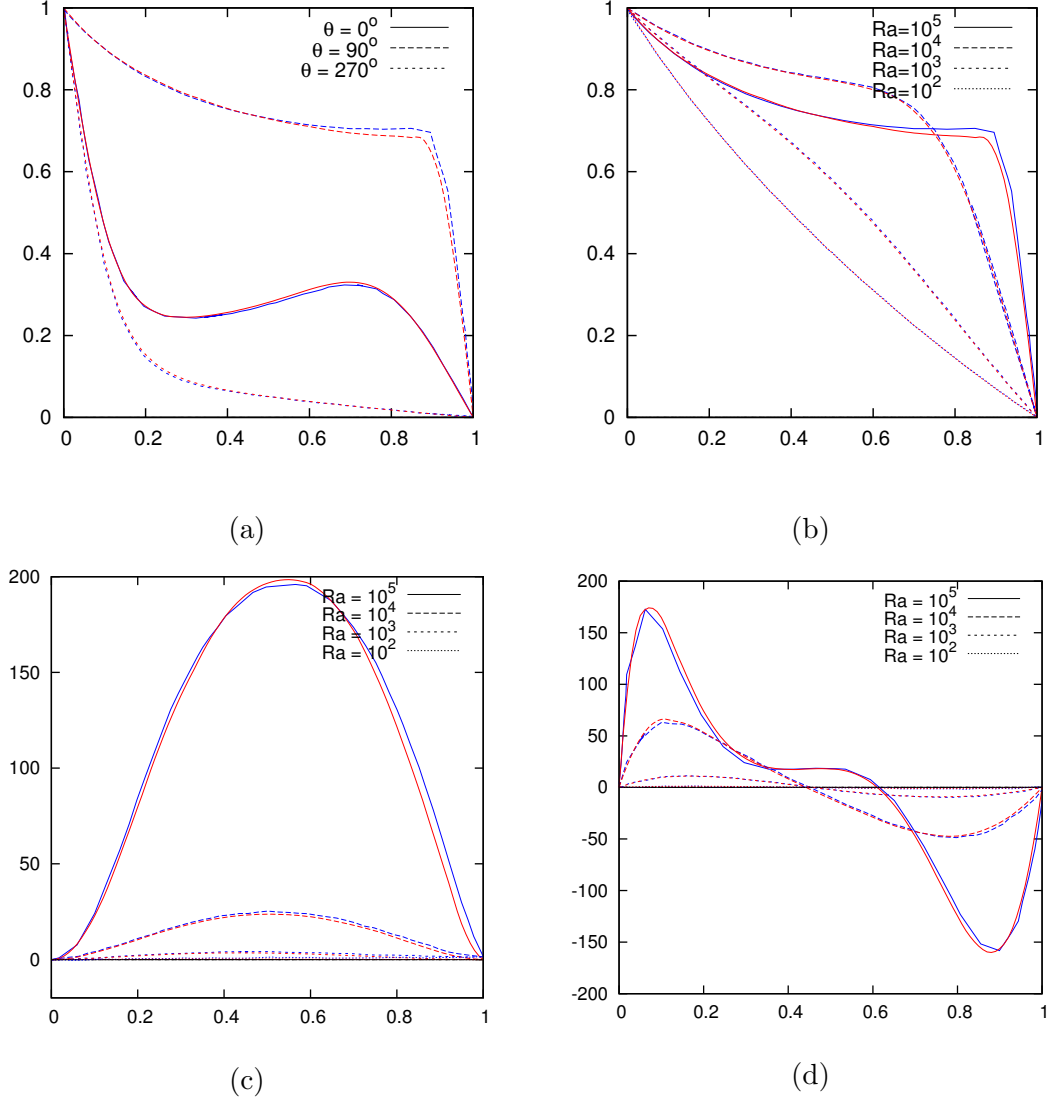
Figure 4.9: Comparison with Padilla et al. (2006) (lines in red are from present work and lines in blue are from the referred work): (a) temperature distribution at $Ra = 10^5$; (b) temperature distribution at $\theta = 90°$; (c) radial velocity profile at $\theta = 90°$;(d) angular velocity profile at $\theta = 0°$

Chapter 5

Concluding Marks

The Ph.D. work contains two main parts: (1) to develop an accurate numerical method for multiphase flow with temperature effects; (2) to apply such method on non-isothermal multiphase flows. This report documented the work within the first part, including developing isoparametric method for accurate representation of the curved boundary and solving the coupling of heat transfer and fluid motion. The key achievement in this report are listed below:

(1) We have proved that theoretically the static solution for a circular bubble at numerical level exists in our numerical method. This is an important finding as very few methods have been proved to possess this property. It will contribute to the suppression of spurious currents, which can cause catastrophic results in the direct numerical simulation of multiphase flow.

(2) In our method, the velocity and temperature of last time step is obtained through tracing the characteristic foot of each nodes, including edge midpoints and vertices. We discussed P2 method of characteristic in 1D situation. When CFL number is small, it can be described as a combination of Beam-Warming scheme and central difference scheme. When CFL number is sufficiently large, the interpolation for the characteristic foot is not certain and hence it is difficult to give a stability analysis on this method. However, our numerical experience shows that this method is stable.

(3) Poisson solvers for 2D and axisymmetric geometries has been validated. Both non-isoparametric P2 and isoparametric P2 method show second order convergence: the numerical error reduces with the increasing number of triangles in

the order of two.

(4) Isoparametric P2 finite element method has been developed in our flow solver on a fixed triangular mesh. The numerical experiments on problems with curved boundaries have confirmed better performance of isoparametric method compared with finite element method with straight edges. The improvement is the result of a more accurate representation of the boundary: in method with straight element edge, the curved boundary is fitted by straight linear segments, while in isoparametric method, the curved boundary is fitted by second-order curved segments.

(5) Convection solver has been validated. The inhomogeneous density induced by temperature variation is dealt with through Boussinesq approximation. The convection and dissipation are handled by firstly solving Navier-Stokes equations and then heat transfer equation. Good agreement with the benchmark solution has been obtained on the natural convection in a square cavity and an annulus.

Chapter 6

Future Plans

This report documented the work on the numerical method. The P2 isoparametric method has been applied on the flow solver for a fixed mesh and the convection solver has been developed. In the development of our numerical method, what remains to be complete are to apply the isoparametric finite element method on a moving mesh and to add the Marangoni stress induced by temperature gradients. The former part includes: (1) the decision of the location of edge midpoints on boundary edges (since we are not only dealing with circular boundary); (2) the interpretation of boundary geometric parameters, including curvature and normal direction; (3) the integration of interfacial boundary conditions over a second-order curved segment. The latter part includes: (1) the representation of Marangoni stress; (2) the interpretation of tangential direction; (3) a better solver for the coupling of heat transfer and fluid motion. Previous studies on thermocapillary instabilities of a liquid layer and single droplet migration with thermocapillarity can be used to validate our numerical method.

Once the numerical method is completed and validated, it can be utilised to investigate general multiphase flows with temperature variation with a 2D or axisymmetric geometry. Capillary jet and droplet dynamics with temperature effects are our specific interest. Capillary jet breakup, droplet collision and droplet spreading are selected as these problems can be modelled in axisymmetric geometry. According to the literature review, some aspects of these problems have not yet been studied thoroughly. For instance, what is the role temperature gradients play in the satellite droplet formation in thermocapillary jet breakup? Does tem-

perature affect whether droplet collision leads to merging or non-merging? and why does non-isothermal droplet spreading with a sufficiently large contact angle have different results compared to that with small contact angle? Our research on multiphase flow with temperature effects will be focused on answering these questions.

A brief plan for the future work and corresponding estimated timing is listed in Table 6.1:

No.	Work	Estimated timing
1	Isoparametric method on moving mesh	09/2015 - 10/2015
2	Thermal induced surface tension variation	11/2015 -12/2015
3	Validation	01/2016
4	Non-isothermal jet breakup	02/2016 - 06/2016
5	Non-isothermal droplet collision	07/2016 - 12/2016
6	Non-isothermal droplet spreading	01/2017 - 06/2017
7	Thesis	06/2017 -09/2017

Table 6.1: Programme of the research, including estimate of timing and dates

Bibliography

J. L. Anderson. Droplet interactions in thermocapillary motion. *International Journal of Multiphase Flow*, 11(6):813–824, 1985. 10

O. A. Basaran, H. Gao, and P. P. Bhat. Nonstandard inkjets. *Annual Review of Fluid Mechanics*, 45:85–113, 2013. 2

H. F. Bauer. Free liquid surface response induced by fluctuations of thermal marangoni convection. *AIAA Journal*, 22(3):421–428, 1984. 8

H. Bénard. Les tourbillons cellulaires dans une nappe liquide.-méthodes optiques d'observation et d'enregistrement. *Journal de Physique Théorique et Appliquée*, 10(1):254–266, 1901. 6

J. B. Bostwick. Spreading and bistability of droplets on differentially heated substrates. *Journal of Fluid Mechanics*, 725:566–587, 2013. 10

J. U. Brackbill, D. B. Kothe, and C. Zemach. A continuum method for modeling surface tension. *Journal of Computational Physics*, 100(2):335–354, 1992. 13

C. E. Brennen. *Fundamentals of multiphase flow*. Cambridge University Press, 2005. 1

A. Cloot and G. Lebon. A nonlinear stability analysis of the bénard–marangoni problem. *Journal of Fluid Mechanics*, 145:447–469, 1984. 7

M. C. Cross and P. C. Hohenberg. Pattern formation outside of equilibrium. *Reviews of Modern Physics*, 65(3):851, 1993. 8

A. A. Darhuber, J. P. Valentino, J. M. Davis, S. M. Troian, and S. Wagner. Microfluidic actuation by modulation of surface stresses. *Applied Physics Letters*, 82(4):657–659, 2003. 3

S. H. Davis. Buoyancy-surface tension instability by the method of energy. *Journal of Fluid Mechanics*, 39(02):347–359, 1969. 7

S. H. Davis. Rupture of thin liquid films. *Waves on fluid interfaces*, pages 291–302, 1983. 7

S. H. Davis. Thermocapillary instabilities. *Annual Review of Fluid Mechanics*, 19(1):403–435, 1987. 6

S. H. Davis. Interfacial fluid dynamics. *Perspectives in fluid dynamics*, pages 1–51, 2002. 1

G. de Vahl Davis. Natural convection of air in a square cavity: a bench mark numerical solution. *International Journal for Numerical Methods in Fluids*, 3 (3):249–264, 1983. 51

G. de Vahl Davis and I. P. Jones. Natural convection in a square cavity: a comparison exercise. *International Journal for Numerical Methods in Fluids*, 3(3):227–248, 1983. 53

P. Dell'Aversana, J. R. Banavar, and J. Koplik. Suppression of coalescence by shear and temperature gradients. *Physics of Fluids (1994-present)*, 8(1):15–28, 1996. 10

J. Eggers. Nonlinear dynamics and breakup of free-surface flows. *Reviews of Modern Physics*, 69(3):865, 1997. 8

P. Ehrhard. Experiments on isothermal and non-isothermal spreading. *Journal of Fluid Mechanics*, 257:463–483, 1993. 10

P. Ehrhard and S. H. Davis. Non-isothermal spreading of liquid drops on horizontal plates. *Journal of Fluid Mechanics*, 229:365–388, 1991. 10

R. W. Faidley and R. L. Panton. Measurement of liquid jet instability induced by surface tension variations. *Experimental Thermal and Fluid Science*, 3(4): 383–387, 1990. 9

L. Fuchs and N. Tillmark. Numerical and experimental study of driven flow in a polar cavity. *International Journal for Numerical Methods in Fluids*, 5(4): 311–329, 1985. 49

S. Ganesan, G. Matthies, and L. Tobiska. On spurious velocities in incompressible flow problems with interfaces. *Computer Methods in Applied Mechanics and Engineering*, 196(7):1193–1202, 2007. 14, 15

J. F. Gerbeau, C. Le Bris, and M. Bercovier. Spurious velocities in the steady flow of an incompressible fluid subjected to external forces. *Oceanographic Literature Review*, 1(45):192, 1998. 14

P. S. Glockner and G. F. Naterer. Thermocapillary control of microfluidic transport with a stationary cyclic heat source. *Journal of Micromechanics and Microengineering*, 15(12):2216, 2005. 3

M. S. Gockenbach. *Understanding and implementing the finite element method.* Siam, 2006. 18

M. D. Gunzburger. *Finite Element Methods for Viscous Incompressible Flows: A guide to theory, practice, and algorithms.* Elsevier, 1989. 25

H. Haj-Hariri, Q. Shi, and A. Borhan. Thermocapillary motion of deformable drops at finite reynolds and marangoni numbers. *Physics of Fluids (1994-present)*, 9(4):845–855, 1997. 9

M. Herrmann, J.M. Lopez, P. Brady, and M. Raessi. Thermocapillary motion of deformable drops and bubbles. In *Proceedings of the Summer Program*, page 155, 2008. 9

C. W. Hirt, A. A. Amsden, and J. L. Cook. An arbitrary lagrangian-eulerian computing method for all flow speeds. *Journal of Computational Physics*, 14 (3):227–253, 1974. 13

C. Q. Hoard, C. R. Robertson, and A. Acrivos. Experiments on the cellular structure in bénard convection. *International Journal of Heat and Mass Transfer*, 13(5):849–856, 1970. 7

H. J. Keh and L. S. Chen. Droplet interactions in thermocapillary migration. *Chemical Engineering Science*, 48(20):3565–3582, 1993. 10

V. G. Levich and V. S. Krylov. Surface-tension-driven phenomena. *Annual Review of Fluid Mechanics*, 1(1):293–316, 1969. 1

J. Li. An arbitrary lagrangian eulerian method for three-phase flows with triple junction points. *Journal of Computational Physics*, 251:1–16, 2013. 35

F. Mashayek and N. Ashgriz. Nonlinear instability of liquid jets with thermocapillarity. *Journal of Fluid Mechanics*, 283:97–123, 1995. 8

M. Meyyappan and R. S. Subramanian. The thermocapillary motion of two bubbles oriented arbitrarily relative to a thermal gradient. *Journal of Colloid and Interface Science*, 97(1):291–294, 1984. 10

M. Meyyappan, W. R. Wilcox, and R. S. Subramanian. The slow axisymmetric motion of two bubbles in a thermal gradient. *Journal of Colloid and Interface Science*, 94(1):243–257, 1983. 9

S. Nas and G. Tryggvason. Thermocapillary interaction of two bubbles or drops. *International Journal of Multiphase Flow*, 29(7):1117–1135, 2003. 9, 10

D. A. Nield. Surface tension and buoyancy effects in cellular convection. *Journal of Fluid Mechanics*, 19(03):341–352, 1964. 7

E. L. M. Padilla, R. Campregher, and A. da Silveira Neto. Numerical analysis of the natural convection in horizontal annuli at low and moderate ra. *CEP*, 38400:902, 2006. 53, 55

J. R. A. Pearson. On convection cells induced by surface tension. *Journal of Fluid Mechanics*, 4(05):489–500, 1958. 6

D. S. Pillai, P. Narayanan, S. Pushpavanam, T. Sundararajan, A. J. Sudha, and P. Chellapandi. A nonlinear analysis of the effect of heat transfer on capillary jet instability. *Physics of Fluids (1994-present)*, 24(12):124106, 2012. 9

S. Popinet and S. Zaleski. A front-tracking algorithm for accurate representation of surface tension. *International Journal for Numerical Methods in Fluids*, 30 (6):775–793, 1999. 13, 14

A. Prosperetti and G. Tryggvason. *Computational methods for multiphase flow.* Cambridge university press, 2007. 11

S. Quan. Simulations of multiphase flows with multiple length scales using moving mesh interface tracking with adaptive meshing. *Journal of Computational Physics*, 230(13):5430–5448, 2011. 13

D. Quéré. Leidenfrost dynamics. *Annual Review of Fluid Mechanics*, 45:197–215, 2013. 11

Lord Rayleigh. Lix. on convection currents in a horizontal layer of fluid, when the higher temperature is on the under side. *The London, Edinburgh, and Dublin Philosophical Magazine and Journal of Science*, 32(192):529–546, 1916. 6

Y. Renardy and M. Renardy. Prost: a parabolic reconstruction of surface tension for the volume-of-fluid method. *Journal of Computational Physics*, 183(2): 400–421, 2002. 13, 14

R. J. Riley and G. P. Neitzel. Instability of thermocapillary–buoyancy convection in shallow layers. part 1. characterization of steady and oscillatory instabilities. *Journal of Fluid Mechanics*, 359:143–164, 1998. 7

J. W. Scanlon and L. A. Segel. Finite amplitude cellular convection induced by surface tension. *Journal of Fluid Mechanics*, 30(01):149–162, 1967. 7

R. Scardovelli and S. Zaleski. Direct numerical simulation of free-surface and interfacial flow. *Annual Review of Fluid Mechanics*, 31(1):567–603, 1999. 13

M. F. Schatz and G. P. Neitzel. Experiments on thermocapillary instabilities. *Annual Review of Fluid Mechanics*, 33(1):93–127, 2001. 8

L. E. Scriven and C. V. Sternling. The marangoni effects. *Nature*, 187:186 – 188, 1960. 2

M. K. Smith. Instability mechanisms in dynamic thermocapillary liquid layers. *Physics of Fluids (1958-1988)*, 29(10):3182–3186, 1986. 7

M. K. Smith. The nonlinear stability of dynamic thermocapillary liquid layers. *Journal of Fluid Mechanics*, 194:391–415, 1988. 7

M. K. Smith and S. H. Davis. Instabilities of dynamic thermocapillary liquid layers. part 1. convective instabilities. *Journal of Fluid Mechanics*, 132:119–144, 1983a. 7

M. K. Smith and S. H. Davis. Instabilities of dynamic thermocapillary liquid layers. part 1. convective instabilities. *Journal of Fluid Mechanics*, 132:145–162, 1983b. 7

Y. Sui. Moving towards the cold region or the hot region? thermocapillary migration of a droplet attached on a horizontal substrate. *Physics of Fluids (1994-present)*, 26(9):092102, 2014. 11

Y. Sui and P. D. M. Spelt. Non-isothermal droplet spreading/dewetting and its reversal. *Journal of Fluid Mechanics*, 776:74–95, 2015. 11

R. L. Thompson, K. J. DeWitt, and T. L. Labus. Marangoni bubble motion phenomenon in zero gravity. *Chemical Engineering Communications*, 5(5-6): 299–314, 1980. 9

G. Tryggvason, B. Bunner, A. Esmaeeli, D. Juric, N. Al-Rawahi, W. Tauber, J. Han, S. Nas, and Y. Jan. A front-tracking method for the computations of multiphase flow. *Journal of Computational Physics*, 169(2):708–759, 2001. 13

Stephen J Vanhook, Michael F Schatz, JB Swift, WD McCormick, and Harry L Swinney. Long-wavelength surface-tension-driven bénard convection: experiment and theory. *Journal of Fluid Mechanics*, 345:45–78, 1997. 7

D. Villers and J. K. Platten. Coupled buoyancy and marangoni convection in acetone: experiments and comparison with numerical simulations. *Journal of Fluid Mechanics*, 234:487–510, 1992. 7

J. Xu and S. H Davis. Liquid bridges with thermocapillarity. *Physics of Fluids (1958-1988)*, 26(10):2880–2886, 1983. 8

J. Xu and S. H. Davis. Convective thermocapillary instabilities in liquid bridges. *Physics of Fluids (1958-1988)*, 27(5):1102–1107, 1984. 8

J. Xu and S. H. Davis. Instability of capillary jets with thermocapillarity. *Journal of Fluid Mechanics*, 161:1–25, 1985. 8

A. L. Yarin, W. Liu, and D. H. Reneker. Motion of droplets along thin fibers with temperature gradient. *Journal of Applied Physics*, 91(7):4751–4760, 2002. 11

G. Yi, T. Thorsen, V. N. Manoharan, M. Hwang, S. Jeon, D. J. Pine, S. R. Quake, and S. Yang. Generation of uniform colloidal assemblies in soft microfluidic devices. *Advanced Materials*, 15(15):1300–1304, 2003. 3

Z. Yin and Q. Li. Thermocapillary migration and interaction of drops: two non-merging drops in an aligned arrangement. *Journal of Fluid Mechanics*, 766: 436–467, 2015. 10

N. O. Young, J. S. Goldstein, and M. J. Block. The motion of bubbles in a vertical temperature gradient. *Journal of Fluid Mechanics*, 6(03):350–356, 1959. 9

F. Zhao, M. Lai, and D. L. Harrington. Automotive spark-ignited direct-injection gasoline engines. *Progress in energy and combustion science*, 25(5):437–562, 1999. 3